NASA TECHNICAL MEMORANDUM

NASA TM X-53063

AUGUST 17, 1964

N64-30510
(ACCESSION NUMBER)
77
(PAGES)
TMX-53063
(NASA CR OR TMX OR AD NUMBER)
FACILITY FORM 602
1
(THRU)
(CODE)
23
(CATEGORY)

NASA TM X-53063

THE CALCULATION OF PROTON PENETRATION AND DOSE RATES

by MARTIN O. BURRELL
Research Projects Laboratory

NASA

George C. Marshall Space Flight Center, Huntsville, Alabama

OTS PRICE

XEROX $ 3.00

MICROFILM $ .75 mF

TECHNICAL MEMORANDUM X-53063

THE CALCULATION OF PROTON PENETRATION AND DOSE RATES

by

Martin O. Burrell

George C. Marshall Space Flight Center

Huntsville, Alabama

ABSTRACT

30510

Computational methods are developed to determine the proton energy degradation and flux attenuation as a function of penetration depth in various materials. The primary purpose of this work is to estimate the energy deposition or tissue dose rate at a given depth or on the surface of a shielded object. Detailed analysis of the methods used and their accuracy are a prime part of this study. Numerous comparisons are made with results of other worker's in this field.

Author

TABLE OF CONTENTS

		Page
I.	INTRODUCTION	1
II.	ENERGY SPECTRA OF PRIMARY PROTONS	1
III.	MULTILAYER SHIELDS	18
IV.	NONELASTIC PROTON COLLISIONS AND SECONDARIES	22
V.	PROTON DOSE RATE CALCULATIONS	34
VI.	ISOTROPIC INCIDENT PROTON FLUX ON SLABS	53
VII.	CONCLUSIONS	71

NASA-GEORGE C. MARSHALL SPACE FLIGHT CENTER

TECHNICAL MEMORANDUM X-53063

THE CALCULATION OF PROTON PENETRATION AND DOSE RATES

by

Martin O. Burrell

RESEARCH AND DEVELOPMENT OPERATIONS
RESEARCH PROJECTS LABORATORY

I. INTRODUCTION

There have been several calculational methods developed to determine the proton energy degradation and flux attenuation as a function of penetration depth in various materials, the ultimate purpose being to estimate the energy deposition or dose rate at a given depth or on the surface of a shielded target such as a man. The methods range from fairly simple approximations to complex and tedious numerical methods. However, most of the methods are essentially the same in that they assume the so-called "straight-ahead model." In this model, the assumption is made that energetic protons lose energy by ionization losses associated with the removal of bound electrons in the shield materials,[1] with no subsequent change in particle direction. Elastic scattering is assumed to be strongly in the forward direction with a negligible energy loss and hence is ignored as a slowing-down mechanism. However, in most of these models, an attenuation correction is made for non-elastic collisions that completely remove the primary proton. The degree of sophistication in the non-elastic collision calculation is a function usually of the shield thickness and the subsequent treatment of the secondary particles liberated.

The methods introduced by the writer are in the same category as those discussed above. It is hoped that the innovations presented will help in obtaining reliable solutions in a simpler manner than is now available.

II. ENERGY SPECTRA OF PRIMARY PROTONS

It seems to follow that regardless of the methods or models used, the slowing-down energy loss of the primary protons is assumed to be dependent only on the ionization loss from bound electrons[2] which is given by various modifications of the Bethe-Bloch formula for stopping power;

---

[1] Hydrogen shields should probably be excepted.

[2] An additional discussion on this point may be found in Section IV of this report, "Non-elastic Proton Collisions."

$$S(E) = -\frac{dE}{dX} = \frac{4\pi e^4}{mv^2} N \left[Z \left(\ln \frac{2mv^2}{I} - \ln (1 - \beta^2) - \beta^2 \right) - C \right]_{(1)} ,$$

where E is the kinetic energy of the proton, Z is the atomic number, $V = \beta C$ is the proton velocity, m is the electron mass, N is the number of atoms of the material per cm^3, I is the average ionization potential of the material, and C is a correction term for electron-shell binding.

A quantity of greater utility in many of the computational schemes is the range of a proton which is given by

$$R(E) = \int_0^E \frac{dE'}{S(E')} . \qquad (2)$$

The dimensions of stopping power, $S(E)$, are usually (Mev-cm^2/gm) and therefore for the range the dimensions are (gm/cm^2) from Eq. (2). In order to see how the above quantities enter into the calculation of proton penetration, the following development is presented. Figure 1a illustrates the parameters of the problem, where E denotes the incident energy of a proton and E^* the energy at depth X.

Now if certain liberties are granted it can be seen that the proton energy in going from E to E^* might be represented by an analytical relationship such as

$$E = g(E^*) , \qquad (3)$$

where, obviously, E^* is a function of X. Hence, the proton differential energy flux at depth $X > 0$ may be related to the flux at depth $X=0$ by a simple change of variable technique denoted by

$$\phi_X(E^*)\, dE^* = \phi_o \left\{ g(E^*) \right\} \left| \frac{dg(E^*)}{dE^*} \right| dE^* . \qquad (4)$$

Of course, the practicality of representing the flux at depth X, as shown in Eq. (4), depends on the ability to find a usable relationship between the energy E and E^*. However, the ability to write Eq. (3)

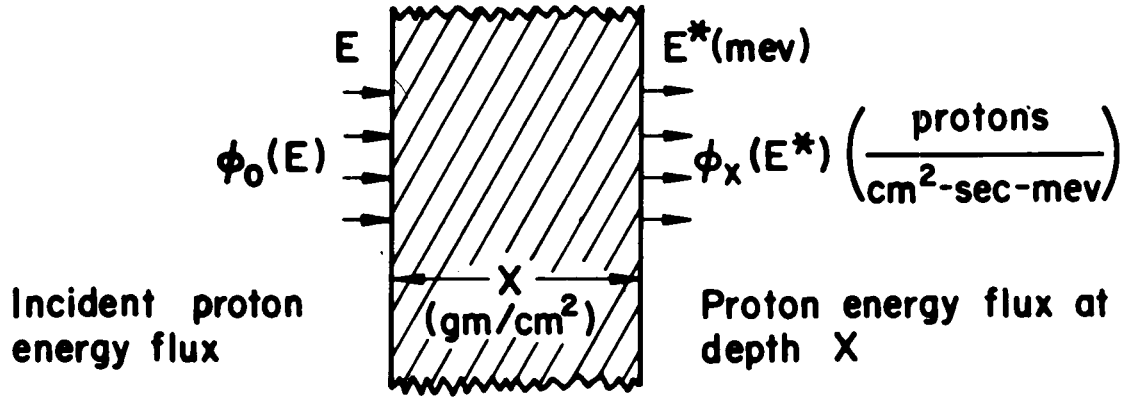

FIGURE 1a. RELATIONSHIP OF PROTON FLUX TO PENETRATION DEPTH

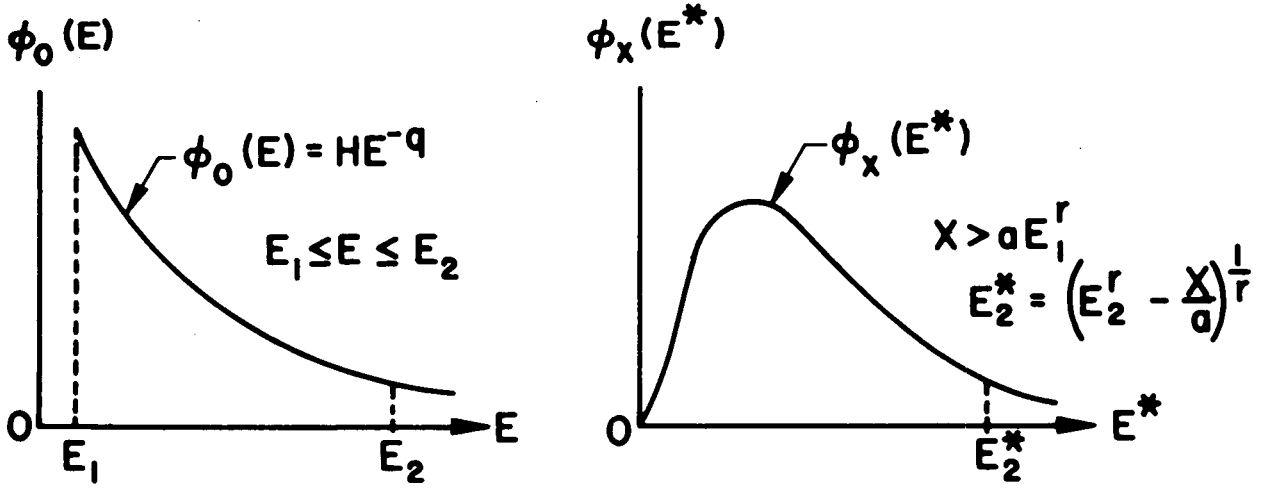

FIGURE 1b. VARIATION OF SPECTRUM SHAPE AS PROTONS PENETRATE A SHIELD

in a nice mathematical expression does not follow from direct application of the Bethe-Bloch formula. In order to arrive at a practical solution to the problem, one can resort to the following exercise in functional manipulation.

The proton range is assumed to be represented by an empirical curve fit, or even as a tabulated set of numbers, in the case of a pure numerical approach. Thus, if

$$R = F_Z(E) \ [\mathrm{gm/cm^2}] \tag{5}$$

is used to denote the range of a proton of energy E incident on a material denoted by the subscript Z, then at the depth X ($\mathrm{gm/cm^2}$) in material "Z", the energy of the proton is reduced by an amount ΔE associated with an equivalent reduction in range given by $\Delta R = X$. Thus we can write

$$R - X = F_Z \ (E - \Delta E) \ . \tag{6}$$

Now $E - \Delta E = E^*$, the energy of the proton at depth X, and since $R = F_Z(E)$ we write

$$F_Z(E) = X + F_Z \ (E^*), \text{ and}$$

$$E = g(E^*) = F_Z^{-1} \ [F_Z \ (E^*) + X] . \tag{7}$$

Thus, Eq. (7) provides the relationship required by Eq. (3). However, there are some obvious restrictions to the functional form which the approximation of $R(E)$ can assume. For this reason, use is often made of the numerical approaches to finding the proton differential energy flux at a depth X. However, it should go without saying that the number of functional forms which are amenable to the manipulations indicated in Eq. (7) are, mathematically speaking, without limits. The most popular attempt to arrive at a simple solution to the proton penetration problem is that given by assuming the range of a proton in a material "Z" can be represented simply by

$$R = a E^r \ , \tag{8}$$

where the coefficient "a" is dependent on the material, and the power "r" only slightly dependent on the "Z" number.[1] In fact, a value of

---

[1] This type of approximation dates back to 1947. R.R. Wilson, Phys. Rev., 71, 385L, Chap. 22, Sec. 3 (1947).

$r \cong 1.78$ will suffice for $Z = 6$ to 30. This choice of range formula is usually considered valid from about 10 to 250 Mev with a maximum error of $\pm$ 5% in approximating the various numerical integrations for range based on the Bethe-Bloch formula for stopping power. As an illustration of the techniques that can be used to arrive at a simple formula for primary proton penetration the following is presented:

Assume that the incident proton energy spectrum is given by

$$\phi_o(E) = HE^{-q} \left[\frac{\text{protons}}{\text{cm}^2\text{-Mev}}\right] ; \quad E_1 \leq E \leq E_2 , \tag{9}$$

and that for the slab thickness and energy spread the range is sufficiently well approximated by Eq. (8); then, from Eq. (7), we write

$$E = g(E^*) = \left(E^{*r} + \frac{X}{a}\right)^{1/r} , \tag{10}$$

from which it is readily seen that

$$E^* = \left(E^r - \frac{X}{a}\right)^{1/r} \quad \text{if} \quad E > \left(\frac{X}{a}\right)^{1/r}$$

and

$$E^* = 0 \quad \text{if} \quad E \leq \left(\frac{X}{a}\right)^{1/r} . \tag{11}$$

From Eq. (11), it follows that if the slab thickness is exactly $X = aE_o^r$, the incident proton of energy E_o will just reach zero energy at depth X. Next we find

$$\frac{dg(E^*)}{dE^*} = \frac{E^{*r-1}}{\left(E^* + \frac{X}{a}\right)^{\frac{r-1}{r}}} . \tag{12}$$

Substituting the appropriate results of Eqs. (9)-(12) into Eq. (4) we obtain

$$\phi_X(E^*) = \frac{HE^{*r-1}}{\left(E^{*r} + \frac{X}{a}\right)^{\frac{r+q-1}{r}}} \; ; \; (E_1^r - \frac{X}{a})^{1/r} \leq E^* \leq (E_2^r - \frac{X}{a})^{1/r} \; , \quad (13)$$

where Eq. (11) must be satisfied for the limits. Figure 1b depicts the general appearance of the transformations between Eqs. (9) and (13).

Equation (13) gives the proton differential energy spectrum at depth X for the incident spectrum given in Eq. (9), if we consider only ionization losses and the range energy equation, $R = aE^r$. At the present the above formulation will be terminated and the improvisions developed by the writer will be undertaken.

The main improvement by the writer is the introduction of an approximation for the proton range which represents the theoretical data, such as presented in Sternheimer's article [1], with an accuracy of $\pm 4\%$, or better, for energies from around 5Mev to over 1,200 Mev. Also, the algebraic manipulation is essentially as elementary as that for the relationship, $R = aE^r$. The new empirical formula for the range is

$$R(E) = \frac{a}{2b} \ln (1 + 2bE^r) \; , \quad (14)$$

where a, b, and r are determined by fitting the range data of Ref. [2] with the requirement to minimize the maximum relative error from 10 to 1000 Mev. If, in Eq. (14), $2bE^r << 1$, then $R \cong aE^r$. For example, in carbon, $r = 1.78$, $a = 2.3 \times 10^{-3}$, and $b = 2 \times 10^{-6}$, and we see that if $E = 200$ Mev, $2bE^r = .05$ and using $R \cong aE^r$ one obtains an error to Eq. (14) of about 2.5%. This good agreement is not obtained, however, with a larger Z number at such a large value of E.

Figure 2 depicts an error analysis of the approximating function of Eq. (14) compared to data presented in Ref. 2 for two different coefficients of r. In general practice it appears that for $Z < 20$, a value of $r = 1.78$ is adequate, and for $Z > 20$, $r \leq 1.75$ should be used. However, in the case of mixed materials of medium and low Z, it seems that a compromise may be made and that for a given calculation, one choice of r adhered to, perhaps 1.78. Table I provides a summary of different values of a and b for different materials with r of 1.75 and 1.78. It should be noted that a value of $r = 1.8$ is also given for tissue; this will be discussed in the development of the methods used by the writer for dose calculations. Figure 3 is a comparison of the error in the range for aluminum when using Eq. (14) to the error in range when using $R = aE^r$. Because of the possible desire to employ other materials than those shown in Table I, the following relationships

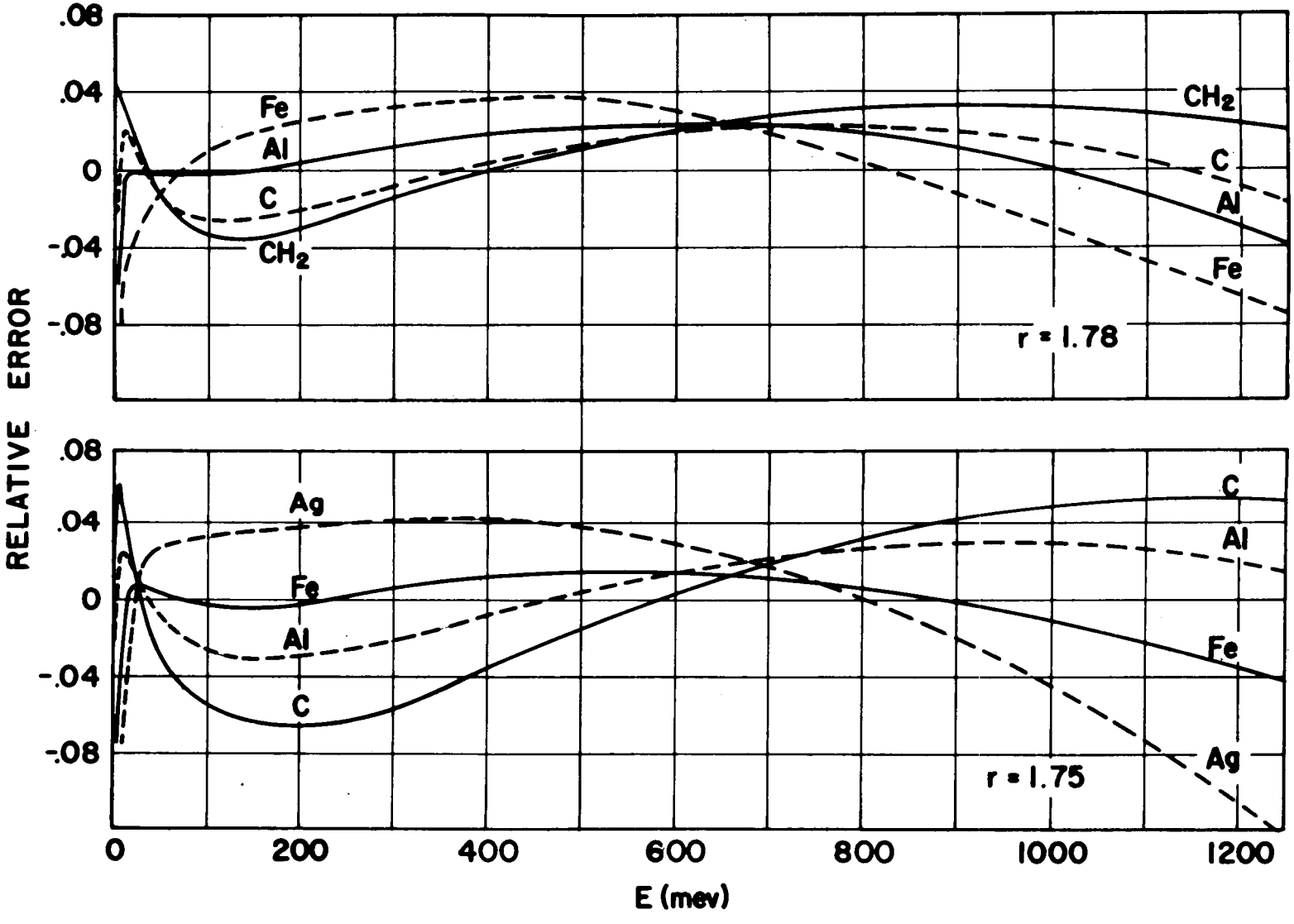

FIGURE 2. THE RELATIVE ERROR IN APPROXIMATING PROTON RANGE USING EQ. (14)

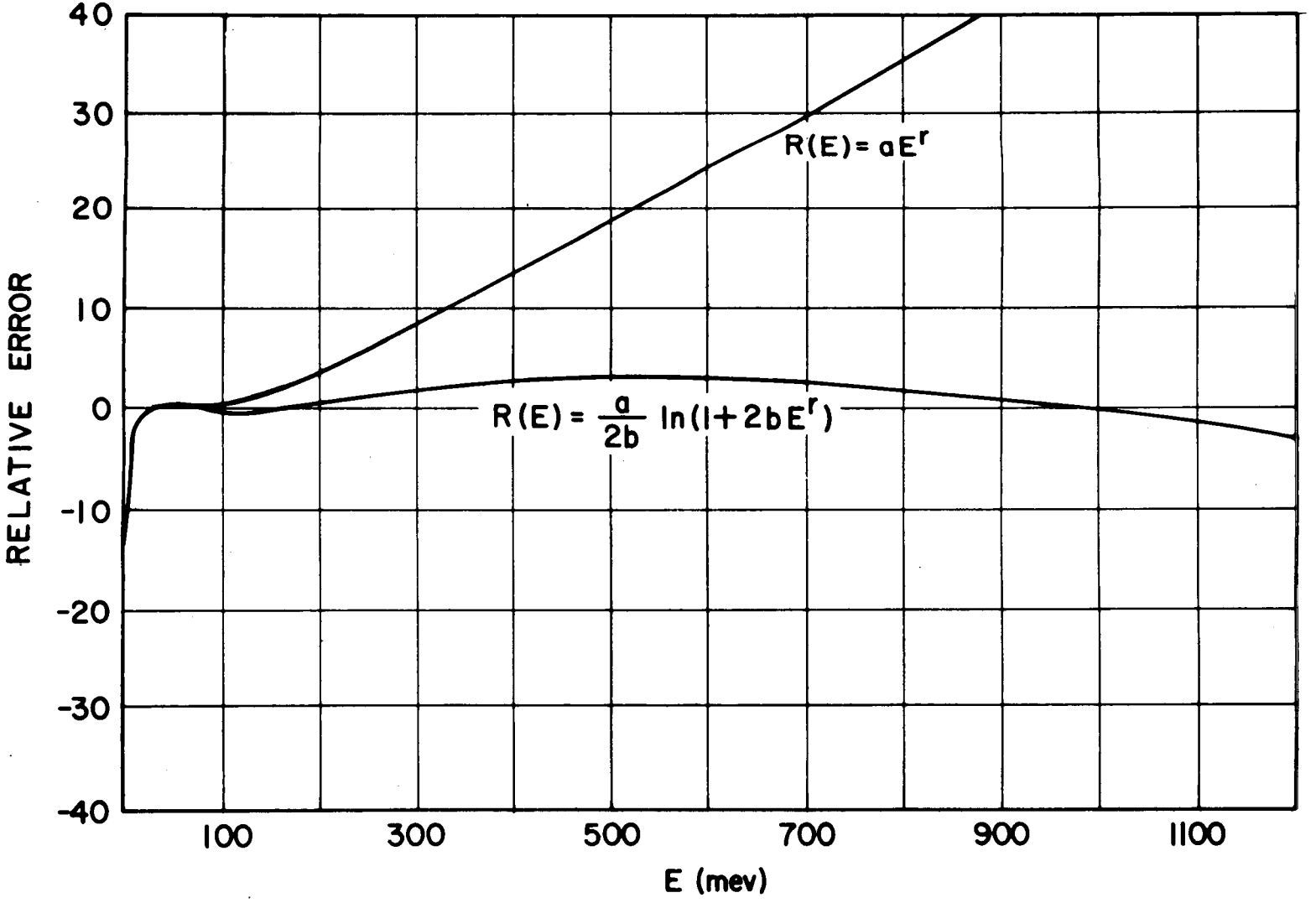

FIGURE 3. COMPARISON OF RELATIVE ERROR IN PROTON RANGE USING EQ. (8) AND EQ. (14)

TABLE I

Coefficients for the Range Equation

	r = 1.75		r = 1.78	
Material	a	b	a	b
Carbon	2.58×10^{-3}	1.2×10^{-6}	2.33×10^{-3}	2.0×10^{-6}
Aluminum	3.10×10^{-3}	1.9×10^{-6}	2.77×10^{-3}	2.5×10^{-6}
Iron	3.70×10^{-3}	2.6×10^{-6}	3.26×10^{-3}	3.0×10^{-6}
Copper	3.85×10^{-3}	2.7×10^{-6}	3.40×10^{-3}	3.25×10^{-6}
Silver	4.55×10^{-3}	3.7×10^{-6}	--------	--------
Tungsten	5.50×10^{-3}	4.2×10^{-6}	--------	--------
Polyethelene	2.15×10^{-3}	1.1×10^{-6}	1.95×10^{-3}	1.7×10^{-6}
Tissue*	2.32×10^{-3}	1.2×10^{-6}	2.11×10^{-3}	2.0×10^{-6}
Water	2.32×10^{-3}	1.2×10^{-6}	2.10×10^{-3}	2.0×10^{-6}
Air	2.68×10^{-3}	1.4×10^{-6}	2.41×10^{-3}	2.1×10^{-6}
SiO_2	2.87×10^{-3}	1.7×10^{-6}	2.58×10^{-3}	2.5×10^{-6}
Glass	3.17×10^{-3}	2.1×10^{-6}	2.83×10^{-3}	2.8×10^{-6}

* For stopping power in tissue: $r_o = 1.80$, $a_o = 1.943 \times 10^{-3}$, $b_o = 2.273 \times 10^{-6}$.

were established by the writer and may be used for obtaining the coefficients a and b when detailed curve fits are not warranted.

$$r = 1.75 \quad \begin{cases} a = 1.6 \times 10^{-3} + 2.89 \times 10^{-4} \sqrt{A} \\ b = 5.16 \times 10^{-7} \sqrt{Z} \end{cases} \tag{15}$$

$$r = 1.78 \quad \begin{cases} a = 1.53 \times 10^{-3} + 2.33 \times 10^{-4} \sqrt{A} \\ b = 8 \times 10^{-7} + 5 \times 10^{-7} \sqrt{Z} \end{cases} \tag{16}$$

where A is the mass number and Z is the atomic number.

The present calculations will be primarily limited to $Z < 20$; hence, for $Z < 20$, we can write the range equation as

$$R(E) = \frac{1.53 \times 10^{-3} + 2.33 \times 10^{-4} \sqrt{A}}{1.6 \times 10^{-6} + 10^{-6} \sqrt{Z}} \ln \left[1 + (1.6 \times 10^{-6} \sqrt{Z}) E^{1.78} \right] . \tag{17}$$

Even though the above equation is best for $Z < 20$, it is found that for practical shielding calculations the value of Z can be extended to about 30 using $r = 1.78$, and the results are quite dependable if the shield thickness is greater than about two gm/cm^2. The reason for this is that in copper ($Z = 29$), for example, the range of a 10-Mev proton is only about 0.025 cm and a 10% error in range (.0025 cm) at this energy is trivial, if compared to the total shield thickness. It should be clear however that at higher energies the range error should be much smaller to maintain the above type of accuracy.

Reverting to the original problem of this section, we develop the following relationships using Eq. (14) for the proton range. From Eq. (7),

$$\frac{a}{2b} \ln (1 + 2bE^r) = X + \frac{a}{2b} \ln (1 + 2bE^{*r}) ,$$

or

$$\ln\left(\frac{1 + 2bE^{r}}{1 + 2bE^{*r}}\right) = \frac{2bX}{a} \quad . \tag{18}$$

Solving for E, we obtain

$$E = g(E^{*}) = (A + BE^{*r})^{1/r} \quad , \tag{19}$$

where

$$B = \exp\left(\frac{2bX}{a}\right) \quad \text{and} \quad A = \frac{1}{2b}(B - 1) \, .$$

From Eq. (19) it follows that

$$E^{*} = \left(\frac{E^{r} - A}{B}\right)^{1/r} \quad \text{if} \quad E > A^{\frac{1}{r}}$$

and

$$E^{*} = 0 \quad \text{if} \quad E \leq A^{1/r} \quad . \tag{20}$$

It is worth noting that if $\frac{2bX}{a} << 1$, then $A \cong X/a$ and $B \cong 1$. (See Eq. 10.) For example, with carbon, $2bX/a = 1.717 \times 10^{-3} X$ and for $X \leq 10$ gm km^2, the above approximation is quite valid. The foregoing analysis demonstrates why the simple range formula ($R = aE^{r}$) gives good results when X is not too large ($X \leq 20$ gm/cm^2 and $E \lesssim 250$ Mev).[1] Next, the differentiation of $g(E^{*})$ gives

$$\frac{dg(E^{*})}{dE^{*}} = \frac{B\, E^{*\, r-1}}{(A + BE^{*r})^{\frac{r-1}{r}}} \, . \tag{21}$$

Substituting the above into Eq. (4), we obtain

$$\phi_{X}(E^{*}) = \frac{\phi_{o}\left\{g(E^{*})\right\} \; B\, E^{*\, r-1}}{(A + BE^{*r})^{r-1/r}} \quad . \tag{22}$$

[1] See discussion following Eq. (14).

There are two choices of the incident differential energy spectrum in vogue at present; the first is that given by Eq. (9) or else a family of N such curves given by

$$\phi_i(E) = H_i E^{-q_i}, \quad E_i \leq E \leq E_{i+1} \tag{23}$$

where $i = 1, 2, 3, \ldots, N$. The second choice of representation is given by the integral rigidity spectrum

$$N(>p) = N_o e^{-p/p_o} \text{ (protons/cm}^2\text{)}; \quad p > p_1 \tag{24}$$

where p and p_o are in rigidity units of MV (millionvolts). From Eq. (24) the differential rigidity spectrum becomes

$$\phi(p)\,dp = -dN(>p) = \frac{N_o}{p_o} e^{-p/p_o} dp, \quad p > p_1 . \tag{25}$$

In order to represent the above momentum rigidity units in energy (Mev) units, it is sufficient to use the relativistic relationship between variables given by $(pze)^2 = E^2 + 2Em_o$ [1] or

$$p = \sqrt{E^2 + 1876E} \tag{26}$$

where (ze) = 1 electron charge for protons, m_o=938 (the rest mass of the proton in Mev units)[2], p is in MV and E is in Mev. Next, using a change of variable technique, we obtain

$$\phi(E)\,dE = -dN(>p(E)) = \frac{N_o}{p_o} e^{-\frac{p(E)}{p_o}} \left|\frac{dp}{dE}\right| dE, \quad p > p_1, \tag{27}$$

---

[1] Note that ΔV = work/q ; in basic physics, the potential difference is thus defined and, hence, Eq. (26) is dimensionally valid.

[2] m_o = 938.23 to 5 significant figures.

where

$$\frac{dp}{dE} = \left(\frac{E + m_o}{\sqrt{E^2 + 2m_o E}} \right) .$$

Substituting dp/dE into Eq. (27), we obtain

$$\phi(E)\, dE = \frac{N_o (E + 938)}{p_o \sqrt{E^2 + 1876\, E}} \exp \left(- \frac{\sqrt{E^2 + 1876\, E}}{p_o} \right) dE, \quad E > E_1 \tag{28}$$

where

$$E_1 = \sqrt{p_1^2 + (938)^2} - 938 ,$$

and $\phi(E)$ has the units of protons/cm^2 Mev. The validity of the above transformation follows from elementary probability theory of distribution functions or else elementary calculus depending on the readers academic orientation.

Referring to Eq. (22) it is of interest to obtain the proton differential energy spectrum at a depth X using the incident spectrums of Eqs. (23) and (24). Using the incident spectrum of Eq. (23) we obtain:

$$\phi_X(E^*) = \frac{H_i B E^{*r-1}}{(A + B E^{*r})^{\frac{r + q_i - 1}{r}}} ; \left(\frac{E_i^r - A}{B} \right)^{1/r} \leq E^* \leq \left(\frac{E_{i+1}^r - A}{B} \right)^{1/r} \tag{29}$$

where Eq. (20) must be satisfied; $B = \exp(2bX/a)$ and $A = (B-1)/2b$. Using the rigidity spectrum of Eq. (24) we obtain (from Eq. 28):

$$\phi_X(E^*) = \frac{N_o (s + 938)\, B E^{*r-1} \exp(-\sqrt{s^2 + 1876\, s}/p_o)}{p_o s^{r-1} \sqrt{s^2 + 1876\, s}} \tag{30}$$

where

$$s = (A + BE^{*r})^{1/r} ; \quad E^* > \left(\frac{E_1^r - A}{B} \right)^{1/r} \quad \text{and} \quad E_1 = \sqrt{p_1^2 + 879,844} - 938.$$

The use of s was simply to shorten the size of the expression in Eq. (30). Examples of typical differential energy spectra as a function of depth X in aluminum are given in Figs. 4 and 5 illustrating the evaluation of Eqs. (29) and (30).

In the following work, throughout this report, the presentation of proton penetration results (dose, flux, etc.) applies equally well to either plane slabs with a normal incident flux or at the center of spherical shells with an incident isotropic flux. This is due to the straight-ahead nature of the proton slowing down in a media, and the fact that the units of differential flux are protons/cm^2-sec-Mev-steradian. Thus, if both time and direction are integrated out, the units are simply protons/cm^2-Mev and the flux has no directional dependence. However, other information is usually provided concerning the source of the spectral data. If we are told that the spectra is for an omnidirectional flux, then the results apply only to the center of a sphere because of the (4π) factor implicitly contained in the total flux. Otherwise the results are applicable as the reader sees fit.

It is of some interest to note in Figs. 4 and 5 that the spectrum's maximum shifts to the right as the slab thickness increases. It is a simple matter to find the value of E^* at which the spectrum's maximum occurs by solving the following equation for E^*,

$$\frac{\partial \phi_X(E^*)}{\partial E^*} = 0 . \tag{31}$$

For example using Eq. (29) for $\phi_X(E^*)$ one obtains

$$E^*_{max} = \left[\frac{(r-1)\left[1 - \exp\left(-\frac{2bX}{a}\right)\right]}{2bq_i} \right]^{1/r} \cong \left[\frac{(r-1)X}{aq_i} \right]^{1/r} \quad \text{if } \frac{2bX}{a} << 1. \tag{32}$$

Equation (32) is plotted in Fig. 6 for three values of q_i. The slowing down media is aluminum with $r = 1.78$, and $2b/a = 1.8 \times 10^{-3}$.

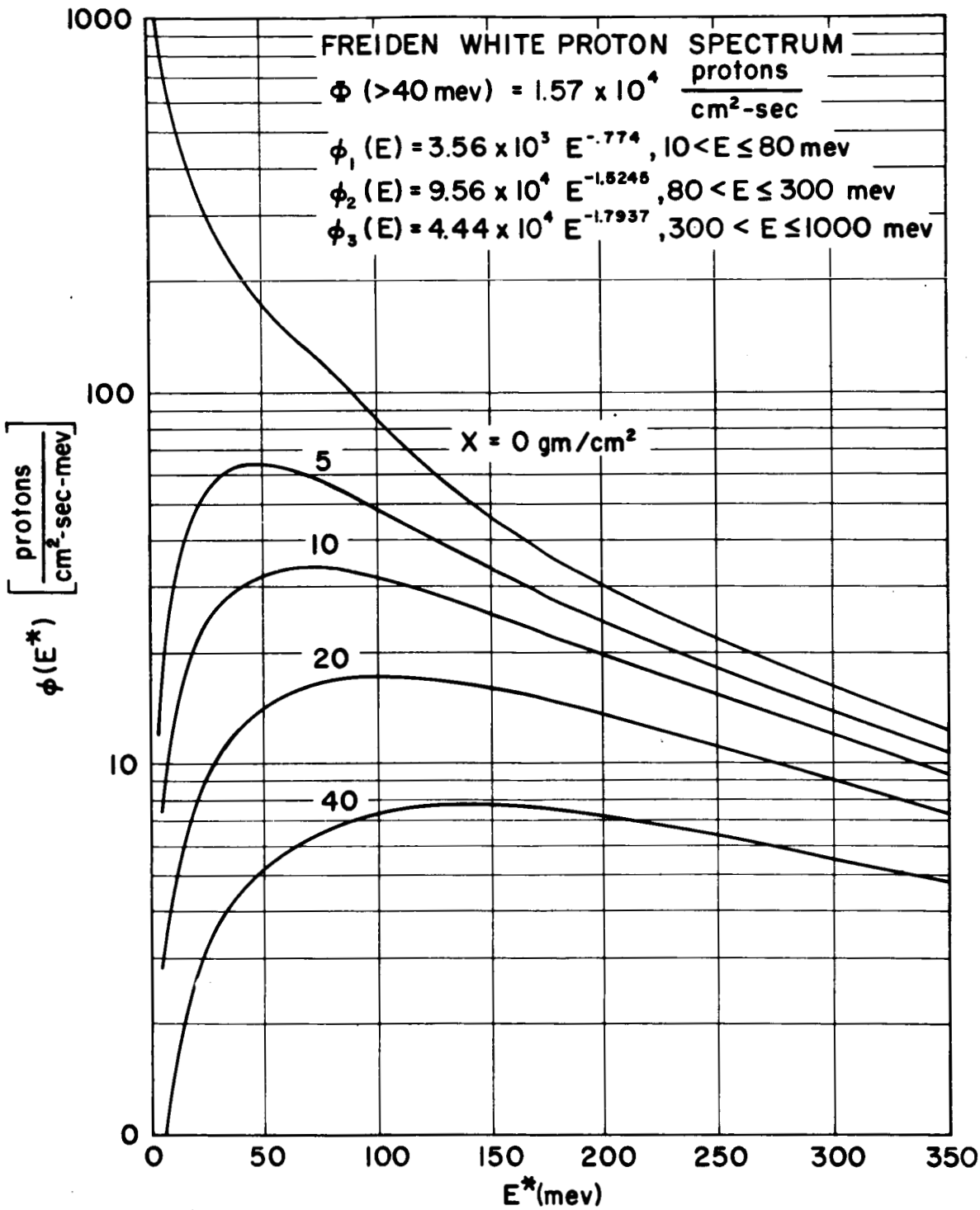

FIGURE 4. PROTON DIFFERENTIAL ENERGY SPECTRUM AT DIFFERENT DEPTHS IN ALUMINUM

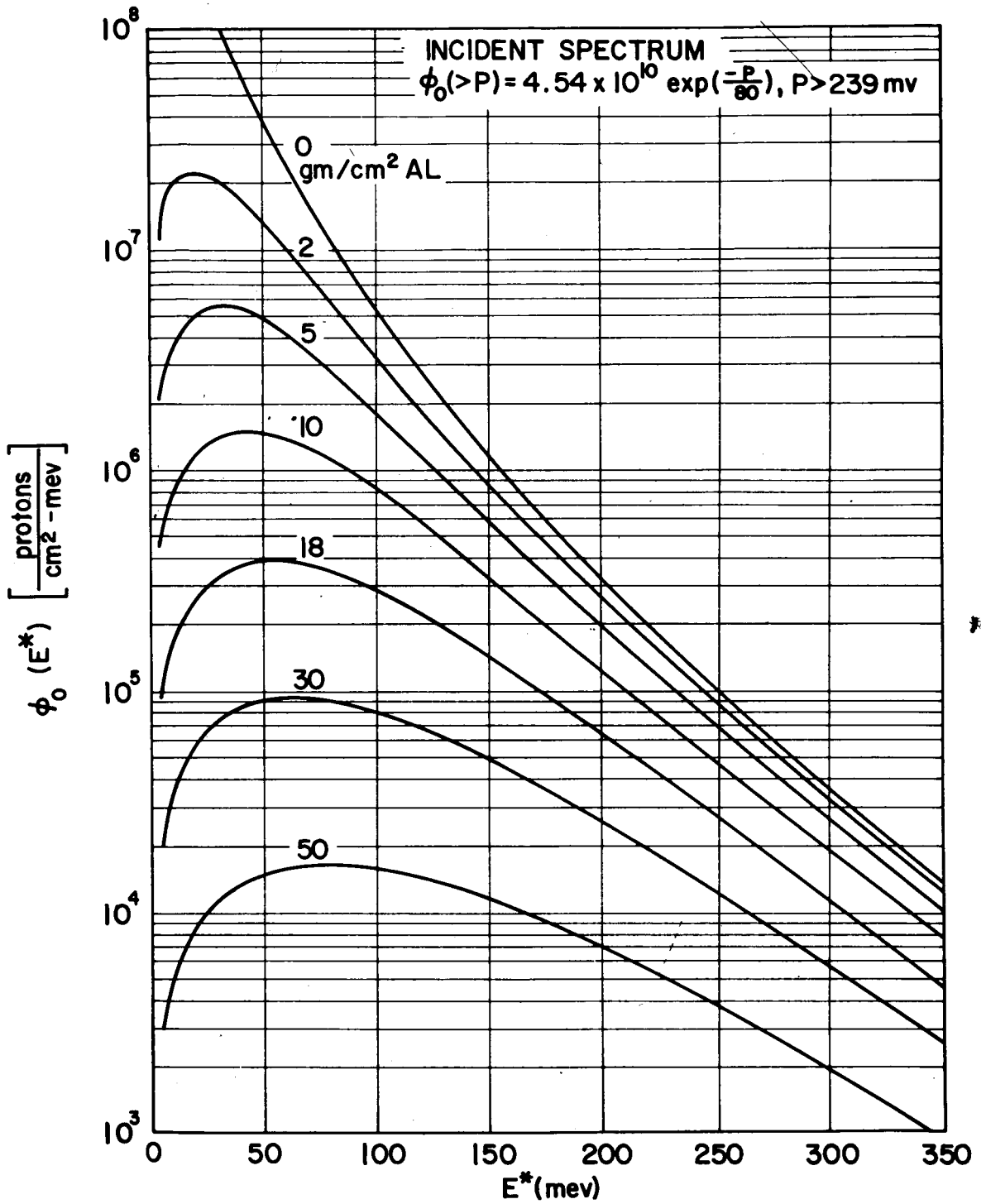

FIGURE 5. PROTON DIFFERENTIAL ENERGY SPECTRUM AT DIFFERENT DEPTHS IN ALUMINUM

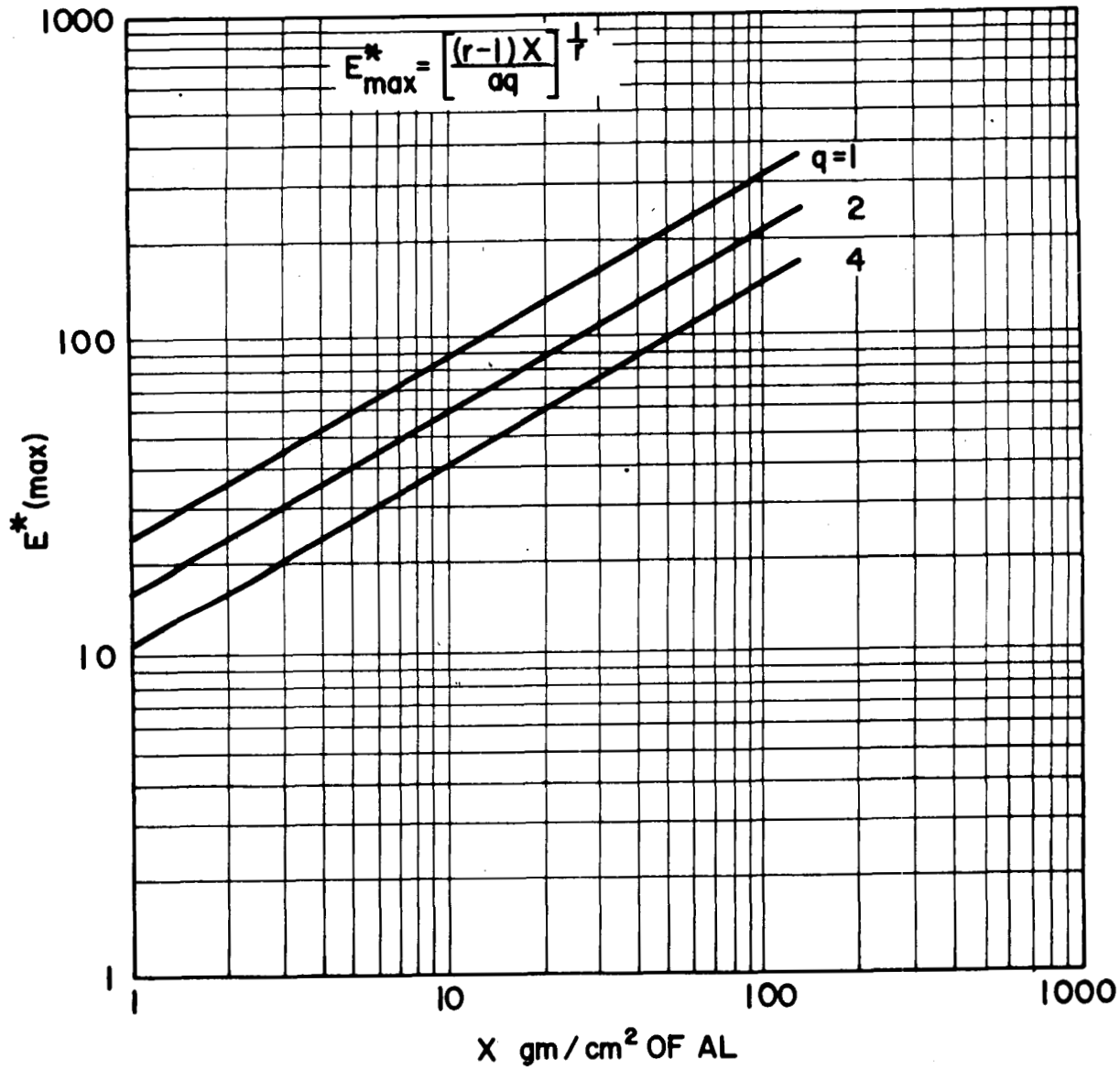

FIGURE 6. ENERGY CORRESPONDING TO MAXIMUM POINT OF DIFFERENTIAL FLUX AS A FUNCTION OF SHIELD THICKNESS AND SPECTRUM COEFFICIENT, q

III. MULTILAYER SHIELDS

The above discussion is equally well applied to stratified layers of different materials. Figure 7 illustrates the parameters involved. In order to see the nature of the derivation for multiple layers of different materials, two layers will be considered initially. Referring to Eq. (19) let us define

$$A_1 = \frac{1}{2b_1}\left[B_1 - 1\right], \quad B_1 = \exp\left(\frac{2b_1X_1}{a_1}\right),$$

and consequently,

$$E_o^r = A_1 + B_1 E_1^r \tag{33}$$

where a_1 and b_1 are the material coefficients of Eq. (14); X_1 refers to the thickness of the first layer with E_o and E_1 denoting the energies respectively incident on the first layer and transmitted through the first layer. Now applying the relationship of Eq. (7) to the second layer, we obtain

$$\frac{a^2}{2b_2} \ln\left(1 + 2b_2 E_1^r\right) = X_2 + \frac{a_2}{2b_2} \ln\left(1 + 2b_2 E_2^r\right);$$

Simplifying,

$$E_1^r = A_2 + B_2 E_2^r \tag{34}$$

where

$$B_2 = \exp\left(\frac{2b_2 X_2}{a_2}\right) \quad \text{and} \quad A_2 = \frac{1}{2b_2}\left[B_2 - 1\right].$$

Substituting E_1^r of Eq. (34) into Eq. (33), we obtain

$$E_o^r = A_1 + B_1(B_2E_2^r + A_2) = (A_1 + B_1A_2) + B_1B_2E_2^r. \tag{35}$$

Equation (35) expresses the energy at a depth of X_2 in the second layer in terms of the energy incident on the first layer. If this

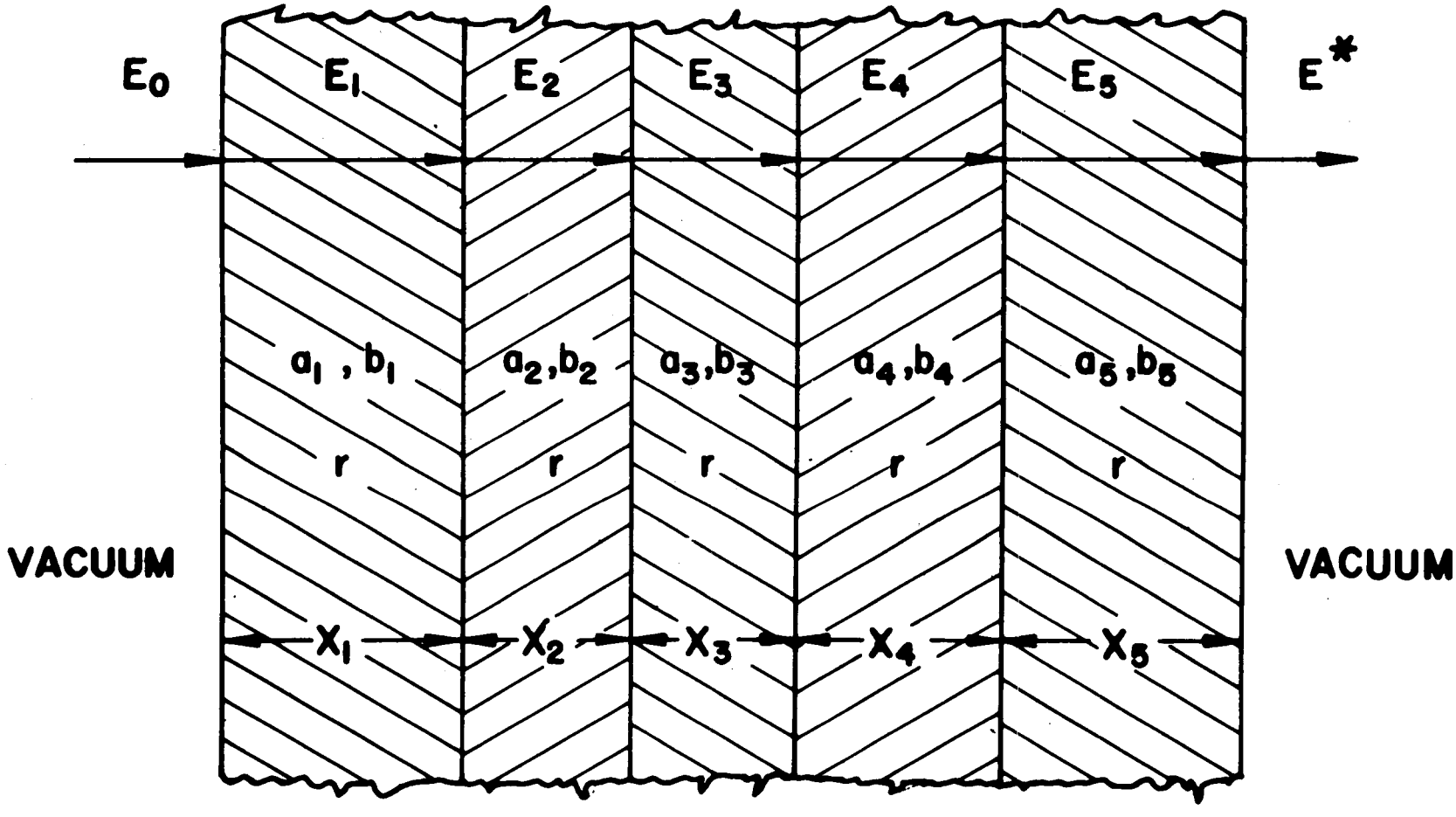

FIGURE 7. MULTILAYER SHIELDS AND ASSOCIATED PARAMETERS

is repeated for N layers one obtains:

$$E^r = A^* + B^* E^{*r} , \tag{36}$$

where E is the incident energy on the first layer and E^* is the energy at the end of the N^{th} layer; and,

$$A^* = A_1 + A_2 B_1 + A_3 B_1 B_2 + \ldots + A_N B_1 B_2 B_3 \ldots B_{N-1} ,$$

$$B^* = B_1 B_2 B_3 \ldots B_N \tag{37}$$

where $B_i = \exp\left(\frac{2b_i X_i}{a_i}\right)$, $A_i = (B_i - 1)/2b_i$, and $i = 1, 2, \ldots, N$. This fairly simple representation of the energy as a function of depth and layer thicknesses of different materials is brought about by the fact that r is assumed to be constant for all materials considered. In shield optimization techniques, such a representation should be promising. Since Eq. (36) has the same form as Eq. (19), it follows that the coefficients A, B may be replaced by A^*, B^* whenever multi-layer shields are considered. Thus, all results obtained in the preceding or subsequent sections can be extended to multiple layers by using A^*, B^* for A, B. In the special case where $2bX/a << 1$, i.e., $(R \cong aE^r)$, then for the ith layer $B_i = 1$, $A_i = X_i/a_i$ and for N layers

$$E^r = E^{*r} + \sum_{r=1}^{N} \left(\frac{X_i}{a_i}\right) . \tag{38}$$

It may be desirable at times to obtain an estimate of the proton transmission for two or more stratified layers of different materials but using only one material for the attenuation. Thus, it is necessary to find the equivalent thickness of the other layers in terms of the base material.

This can be readily done in the following manner. First, we assume that for the base material, the simple power law holds for the range equation $(R = aE^r)$. Then the thickness of the various layers in terms of the base element becomes simply,

$$X^{*}_{\beta} = \left(\frac{a_{\beta}}{a_{A}}\right) X_{A} \quad , \tag{39}$$

where A denotes a mass or material number; a denotes the coefficient of the range equation[1] for the various materials; and the subscript β denotes the base material. For example, if a reliable but simple estimate was desired for the proton dose rate behind 5 gm/cm^2 of Aluminum and 5 gms/cm^2 of tissue, the following information may be read off a plot of dose rates versus depth in aluminum by reading the dose rate at the depth:

$$X^{*}_{Al} = X_{Al} + \frac{a_{Al}}{a_{(tissue)}} X_{tissue}$$

or

$$X^{*}_{Al} = 5 \text{ gm/cm}^2 + \frac{2.77 \times 10^{-3}}{2.11 \times 10^{-3}} \quad (5 \text{ gm/cm}^2) = 11.56 \text{ gm/cm}^2 \tag{40}$$

That the above technique is valid can be shown readily by inserting X^{*}_{β} into Eq. (38), thus obtaining

$$E^{r} = E^{*r} + \frac{X_{\beta}}{a_{\beta}} + \frac{X^{*}_{\beta}}{a_{\beta}} = E^{*r} + \frac{X_{\beta}}{a_{\beta}} + \left(\frac{a_{\beta}}{a_{A}}\right) \frac{X_{A}}{a_{\beta}} \tag{41}$$

or

$$E^{r} = E^{r} + \frac{X_{\beta}}{a_{\beta}} + \frac{X_{A}}{a_{A}} \quad .$$

The last equation denotes the equivalent energy transformation if we had used the material coefficients. Thus, the substitution of Eq. (39) gives the same results as the simple power law approximation of the range equations provided the same power r is used for all the

---

[1] The values of a are taken from Table I.

materials. The utilization of the above simple relationships is of engineering importance for estimating depth dose due to primary protons when only a simple curve is provided for the so-called "skin dose." See Section V on "Proton Dose Rate Calculations."

IV. NONELASTIC PROTON COLLISIONS AND SECONDARIES

It was pointed out in the introduction to this paper that elastic scattering off a nucleus by high energy protons (>20 Mev) is highly forward with trivial reduction in energy. This assumption is not as valid for proton collisions in hydrogen but this problem will not be treated here. However, it is worth mentioning that the so-called range straggling associated with energetic protons is an effect mainly due to elastic collisions with electrons. However, this type of error is usually quite small and can be represented approximately for protons by

$$\sigma_R \cong 0.015\,R \quad , \tag{42}$$

where σ_R is the standard deviation of a Gaussian distribution depicting the statistical fluctuation of the range about a mean range R (p. 662, [3]). This can be interpreted as meaning that 95% of monoenergetic protons should have a measured range within about ± 3% of the theoretical range calculated from ionization losses only. This is not a bad error for shielding calculations since the proton energy spectrum always contains uncertainties of a much greater order of magnitude. This error is also in keeping with the use of the approximation for the range introduced by the writer (Eq. 14). Examination of the error curves in Fig. 2 shows that for energies from less than 10 Mev to over 1000 Mev the coefficients (a, b, r) can be chosen to maintain a maximum variation of less than 4% from an accurate theoretical calculation.

In the treatment of nonelastic cross sections the writer has represented the cross section as a function of energy and mass number using an empirical expression which is amenable to obtaining closed form solutions in the mathematical operations which are necessary to obtain transmitted flux and dose rates. The greatest constraint in obtaining an accurate expression for cross sections is the lack of adequate

experimental nonelastic cross sections in the range of 5 Mev to 50 Mev for protons. There are a few values at widely separated energies. However, the low-energy cross section seems to resemble that of neutrons to some extent and for energies from 5Mev to 18 Mev the nonelastic cross section of neutrons taken from Troubetzkoy [4] were used for the protons with a Coulomb correction in energy. Then the low-energy cross sections were blended into the proton nonelastic cross section at higher energies. For proton energies in the range of 200 to 2000 Mev, the nonelastic cross section is fairly well represented by the theoretical formula of Fernbach, Serber, and Taylor,

$$\sigma_{ne} = \pi R^2 \left[\frac{1 - (1 + 2KR)e^{-2KR}}{2K^2R^2} \right] \text{cm}^2 , \qquad (43)$$

where $R = r_o A^{\frac{1}{3}}$ is the radius of the target nucleus with mass number A, and K^{-1} is the mean free path in nuclear matter. A simpler expression, determined by the author, which agrees well with experimental values, as well as Eq. (43), is given by

$$\sigma_{ne} = 0.38 \left(\frac{A}{27} \right)^{0.73} [\text{barns}] . \qquad (44)$$

The reason for choosing the ratio $(A/27)$ in Eq. (44) is that the nonelastic cross sections for aluminum $(A=27)$ will be the basis for the empirical formulas which are developed below. The requirements for such a formula are that the values of the cross section should be zero at zero energy, have a maximum between 5 and 25 Mev, and be approximately a constant (asymptote) as the energy exceeds say 200 Mev. Equation (45) satisfies these requirements with some degree of success, in addition to being tailored for further mathematical operations:

$$\sigma_{ne}(E) = \frac{0.38 \left(\frac{A}{27} \right)^{0.73} E^{2r} + dE^r}{E^{2r} + fE^r + g} , \qquad (45)$$

where d, f, g are constants to be determined by curve fitting techniques and $r (= 1.78)$ is the same power as used in the range equation, (14).

Examination of Eq. (45) shows that $\sigma_{ne}(0) = 0$. Also, as E becomes large, $\sigma_{ne}(E) \rightarrow .38\,(A/27)^{.73}$; this is readily seen by dividing numerator and denominator of Eq. (45) by E^{2r} and letting E increase without bounds. In order to require that Eq. (45) has a proper maximum for some positive value of $E = E_M$, the derivative of Eq. (45) is equated to zero and Eq. (46) is found;

$$E_M^r = \frac{cg + \sqrt{c^2 g^2 - cdfg + d^2 g}}{d - cf} \quad , \quad d > cf \quad , \qquad (46)$$

where $c = .38\,(A/27)^{.73}$ and the quantity under the radical is ≥ 0. It should be pointed out that Eq. (45) has a minimum for a negative value of E . In the variable E^r, Eq. (45) is a "serpentine" (as encountered in analytic geometry) which has been translated. In general, the type of curve which is represented by Eq. (45) is shown in Fig. 8.

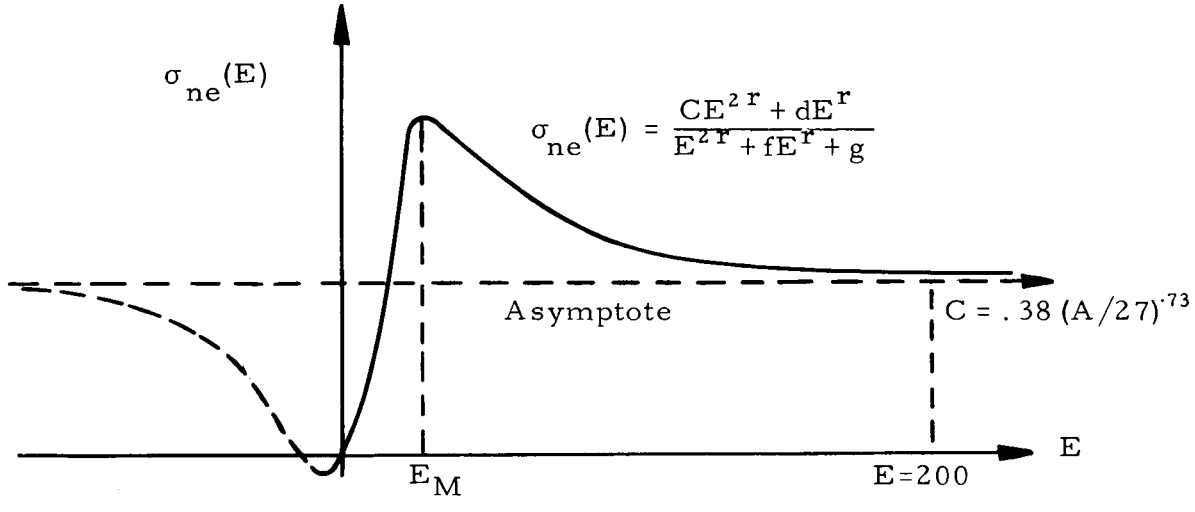

Figure 8. Nonelastic Cross Section Formula

In order to determine the coefficients (d, f, g) of Eq. (45) it is sufficient to solve simultaneously the system of equations given by

$$\text{I)} \quad X_M^2 d - cX_M^2 f - 2c X_M g - dg = 0$$

$$\text{II)} \quad X_M d - \sigma_M X_M f - \sigma_M g = X_n^2 (\sigma_M - c) \qquad (47)$$

$$\text{III)} \quad X_o d - \sigma_o X_o f - \sigma_o g = X_o^2 (\sigma_o - c)$$

where $X = E^{1.78}$ and $c = 0.38 (A/27)^{0.73}$. Equation I is derived from Eq. (46) and Eqs. II and III are from Eq. (45). When A=27 (aluminum), the following coefficients were obtained: $c = .38$; $d = 88$; $f = -85$; $g = 12,000$. The above choice was determined by setting $E_M = 16$ Mev with $\sigma_M = 1$ barn and then requiring $\sigma_o = .15$ barn at $E_o = 5$ Mev. The estimated values of σ_{ne} $(E < 20)$ for protons were found by using the neutron data of Troubetzkoy [4], and applying the relationship

$$\sigma_P(E) = \sigma_n [E - B(z,A)] \; ; \; B(z,A) \cong 1.15 \; z/A^{\frac{1}{3}} \qquad (48)$$

where $B(z,A)$ is the Coulomb potential barrier, E the incident proton energy, and σ_n is the total neutron nonelastic cross section taken from Ref. [4] for aluminum. Since for high energies $(E > 200$ Mev) the total nonelastic cross section is given by the simple formula of Eq. (44), the same sort of expression would be desirable for all energies. Hence the expression below is an attempt to derive such an expression:

$$\sum_{ne} (E,A) = \sigma_{ne}(E) \times \left(\frac{N_o}{A}\right) = \frac{CE^{2r} + dE^r}{E^{2r} + fE^r + g} \; (cm^2/gm), \qquad (49)$$

where

N_o = Avogadro's number
$C = 8.479 \times 10^{-3} (27/A)^{0.27}$,
$r = 1.78$,
$d = 1.9547 (A/27)^{.221 - .27} = 1.9547 (A/27)^{0.12338}$,
$f = -84.9 (A/27)^{.221\, r} = 84.9 (A/27)^{.39338}$, and
$g = 11,996.3 (A/27)^{.442\, r} = 12,000 (A/27)^{.78676}$

The writer makes no claim to success in finding an adequate representation. However, the accuracy of Eq. (49) is probably sufficient for low-Z materials (Z < 30). Figure 9 shows the results of using the above fit for several different A numbers. Figure 10 is for $\sigma_{ne}(E)$ in barns. The reversal of relative values between Fig. 9 and Fig. 10 should be observed.

In order to utilize the above equation in a computation, the following analysis is undertaken. If a proton energy flux $\phi_o(E)$ [protons/cm^2-Mev] is incident on a slab of material, A, and if nonelastic collisions are considered, the energy spectrum of the primary protons which get to a depth $x(gm/cm^2)$ should be given by

$$n_x(E^*) = \phi_x(E^*)\, e^{-\int_o^{x'} \Sigma_{E^*}(x)\, dx} \tag{50}$$

where $\phi_x(E^*)$ is given by expressions such as Eqs. (29) and (30), and $\Sigma_{E^*}(x)$ is given by Eq. (49) with the energy E depending on x according to Eq. (19) or, simply,

$$E = \left(Q e^{\nu x} - \frac{1}{2b}\right)^{1/r} \tag{51}$$

where

$$Q = \left(E^{*r} + \frac{1}{2b}\right) \quad \text{and} \quad \nu = \frac{2b}{a} .$$

The problem hinges on the ability to integrate the exponential of Eq. (50). Hence the expression,

$$\Sigma_{E^*}(x) = \frac{(c - 2bd) - 4b(c - bd)\, Q e^{\nu x} + 4c\, b^2 Q^2 e^{2\nu x}}{1 - 2bf + b^2 g) - 4b(1 - bf)\, Q e^{\nu x} + 4b^2 Q^2 e^{2\nu x}} \tag{52}$$

is obtained by substituting the energy transformation of Eq. (51) into Eq. (49). Now, make the following substitutions:

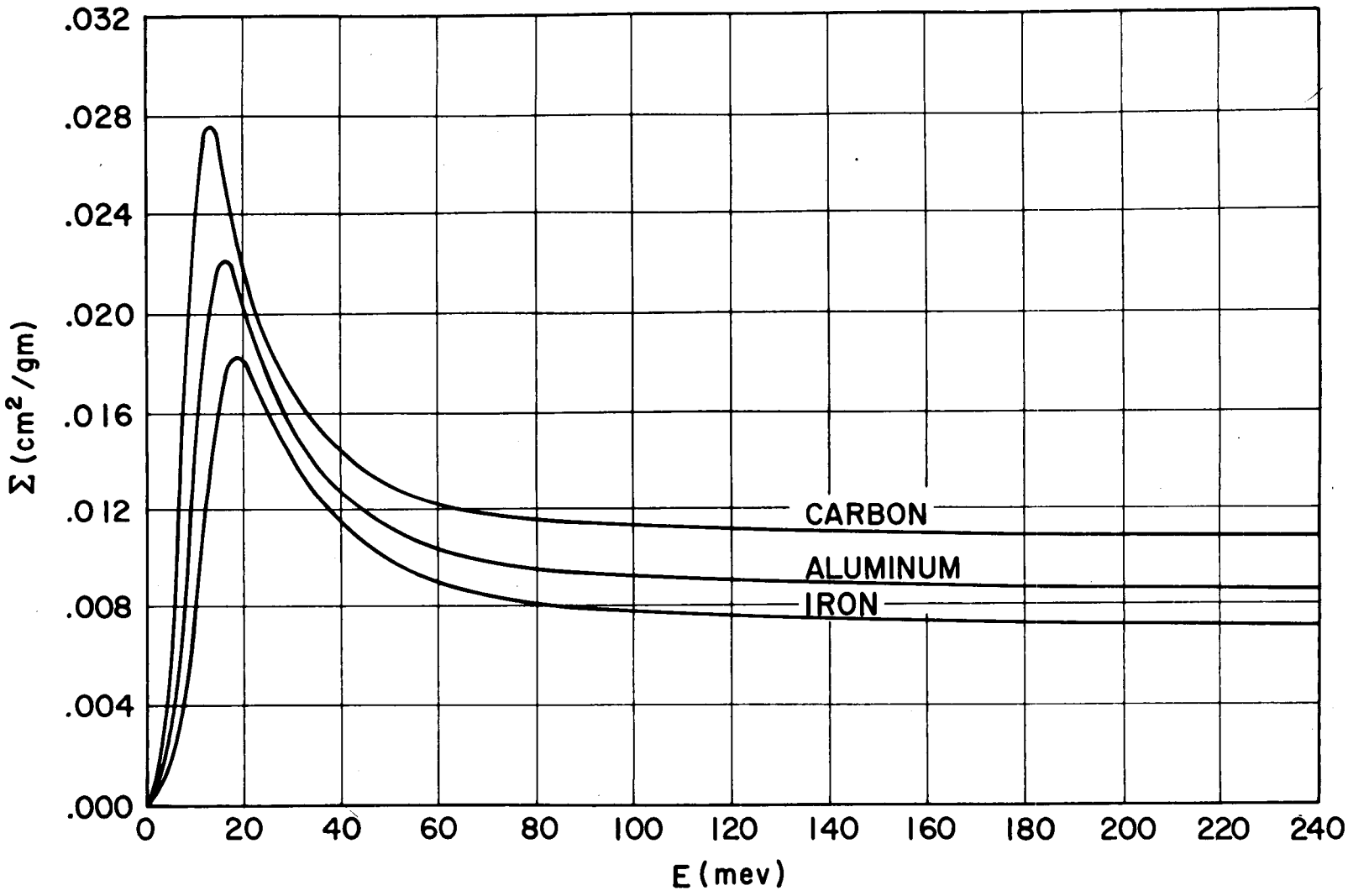

FIGURE 9. PROTON NONELASTIC CROSS SECTIONS IN (CM^2 /GM) UNITS

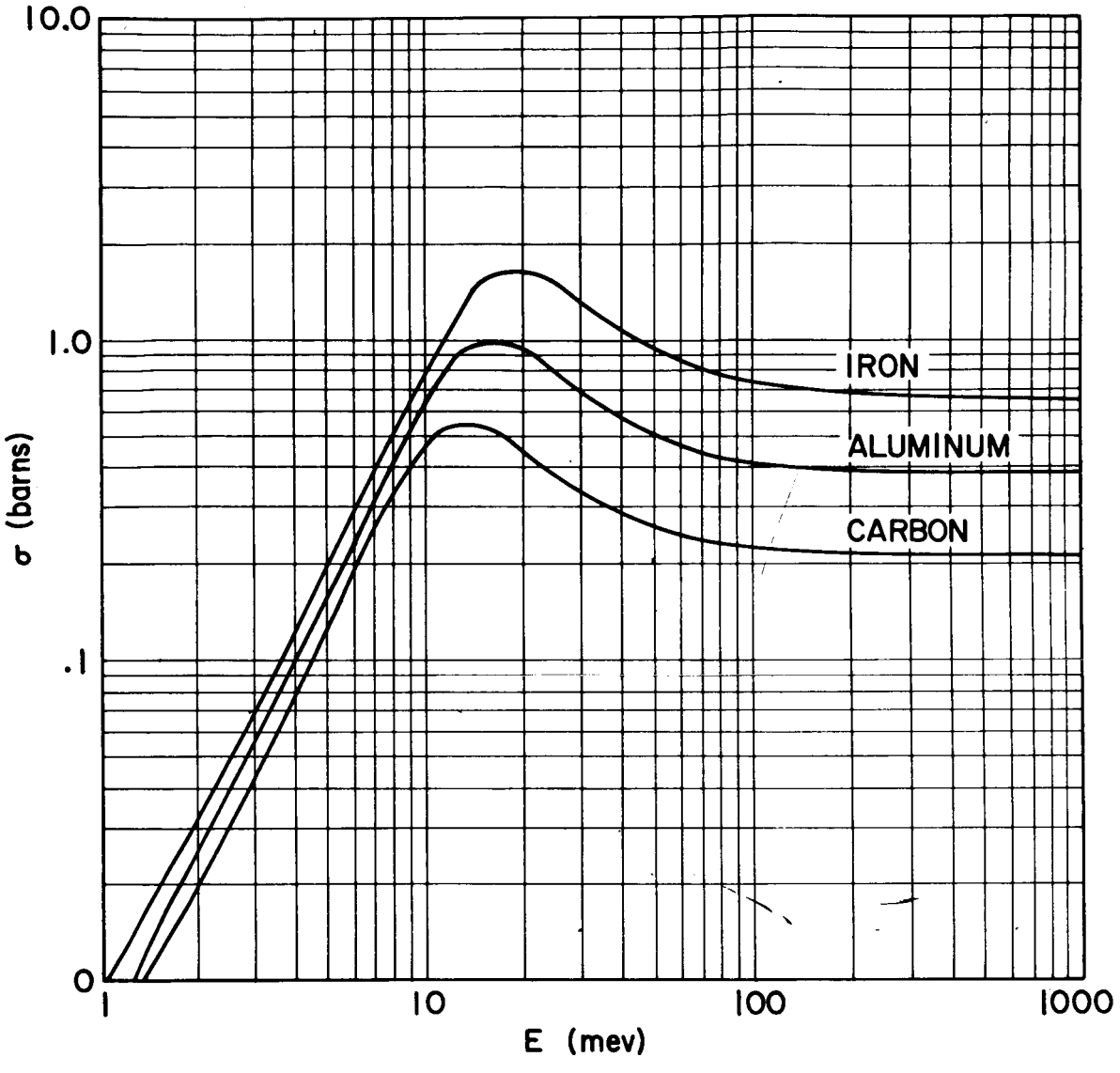

FIGURE 10. PROTON NONELASTIC CROSS SECTIONS IN BARNS/ATOM

$$2bQe^{\nu x} = t \text{ and } dx = \frac{dt}{\nu t} \quad (d \text{ is differential here}) ;$$

$$\omega = c - 2bd ; \quad \theta = c - bd \quad (d \text{ is a constant here}) ;$$

$$\alpha = 1 - 2bf + 4b^2 g ; \text{ and } \beta = 1 - bf .$$

Then the integration of Eq. (52) can be represented by

$$\int_0^{x'} \Sigma_{E^*}(x)\, dx = \frac{1}{\nu} \int_{2bQ}^{t' = 2bQe^{\nu x}} \left(\frac{\omega - 2\theta t + ct^2}{\alpha - 2\beta t + t^2} \right) \frac{dt}{t} . \quad (53)$$

letting $T = \alpha - 2\beta t + t^2$, we can write

$$\int_0^{x'} \Sigma_{E^*}(x)\, dx = \frac{\omega}{\nu} \int_{2bQ}^{t'} \frac{dt}{tT} - \frac{2\theta}{\nu} \int_{2bQ}^{t'} \frac{dt}{T} + \frac{c}{\nu} \int_{2bQ}^{t'} \frac{tdt}{T} . \quad (54)$$

Equation (54) is now a set of standard forms in most handbooks. However, one observation should be made about the expression

$$q = 4\alpha - 4\beta^2 = 4b^2 (4g - f^2) , \quad (55)$$

where the q , as defined above, occurs in the handbook solutions to Eq. (54). Since the factor $\sqrt{q}$ occurs in the handbook formulas, it should be noted that

$$4g > f^2 \quad (56)$$

must be satisfied in order to obtain a valid solution. This inequality is readily satisfied as seen by examination of Eq. (49). Also, this inequality determines the nature of the solution since a solution is obtainable for $\sqrt{-q}$ but with a different mathematical form. Thus we obtain for the solution of Eq. (54), omitting details of simplification:

$$\int_0^{x'} \Sigma_{E^*}(x)\,dx = DX + \log\left[\frac{G^2 + (A + \frac{f}{2} + BE^{*r})^2}{G^2 + (\frac{f}{2} + E^{*r})^2}\right]^{\frac{a}{4b}(C-D)}$$

$$+ F\left[\tan^{-1}\left(\frac{A + \frac{f}{2} + BE^{*r}}{G}\right) - \tan^{-1}\left(\frac{\frac{f}{2} + E^{*r}}{G}\right)\right] \quad (57)$$

where

$$D = \frac{C - 2bd}{1 - 2bf + 4b^2 g}\,, \quad G = \sqrt{g - \frac{f^2}{4}}$$

and

$$F = \frac{a}{4bG}\left[f(D - C) - 4bgD\right]\,.$$

The definitions of A and B are given in Eq. (19). The value of F is approximately 3.35×10^{-4} for aluminum. Hence there appears to be some justification for dropping the arctan functions. That this assumption is valid will be shown below. In any case we can write

$$e^{-\int_0^{x'} \Sigma_{E^*}(x)dx} = \left[\frac{G^2 + (\frac{f}{2} + E^{*r})^2}{G^2 + (A + \frac{f}{2} + BE^{*r})^2}\right]^{\frac{a}{4b}(C-D)}$$

$$\times \exp\left\{-DX - F\left[\tan^{-1}\left(\frac{A + \frac{f}{2} + BE^{*p}}{G}\right) - \tan^{-1}\left(\frac{\frac{f}{2} + E^{*n}}{G}\right)\right]\right\} \quad (58)$$

of simply if F times the difference in the arctan functions is sufficiently small;

$$e^{-\int \Sigma_{E^*(x)}\,dx} = \left[\frac{G^2 + \left(\frac{f}{2} + E^{*r}\right)^2}{G^2 + \left(A + \frac{f}{2} + BE^{*r}\right)^2}\right]^{\frac{a}{4b}(C - D)} e^{-DX} . \qquad (59)$$

Figure 11 is presented in order to illustrate the integral over penetration depth of the differential nonelastic cross section of the proton slowing down from ionization losses and also the effect on the cross sections of the arctan terms in Eq. (57). The curves in Fig. 11 are simply the integral of Eq. (57) divided by the depth x of penetration in aluminum. These curves depict the energy dependence of the nonelastic cross sections and exemplifies dramatically the effects of the ionization losses. The dashed curves show the results obtained when the arctan terms are omitted. It should be noted that the cross sections are plotted as a function of the protons energy E^* at the depth X in aluminum. Perhaps the next curve, Fig. 12, presents the most significant results of the foregoing analysis. Here Eq. (58) is plotted for the same thicknesses as shown in Fig. 11. Rather interesting is the fact that the exponential function (Eq. 58 or 59) is very nearly a constant over the total energy range for a given penetration thickness. This is a very important demonstration since the examination of Fig. 11 might lead one to infer that the use of Eq. (57) or equivalent is necessary in order to obtain a reliable flux calculation for penetration thicknesses less than say 10 gm/cm^2. Actually, the relative errors associated with using a constant cross section increase with depth so that at a depth of 50 grams/cm^2 the error in the attenuation is of greater significance than at 2 gm/cm^2. The major problem associated with choosing a constant cross section is the cross section dependence on a given proton energy spectrum. However, it is felt that an approximation such as given in Eq. (60) below is justified in view of the many uncertainties that exist in any energy spectrum or the total proton intensity.

$$\overline{\overline{\sum}}_{ne}(A) \cong 0.01 \left(\frac{27}{A}\right)^{0.27} \left[\frac{cm^2}{gm}\right] . \qquad (60)$$

In Eq. (60) the constant, .01, may be reduced to .009 or less when $X \gtrsim 20$ gm/cm^2. However, the nonelastic cross section, as given by Eq. (60), should be restricted for application to the attenuation of the

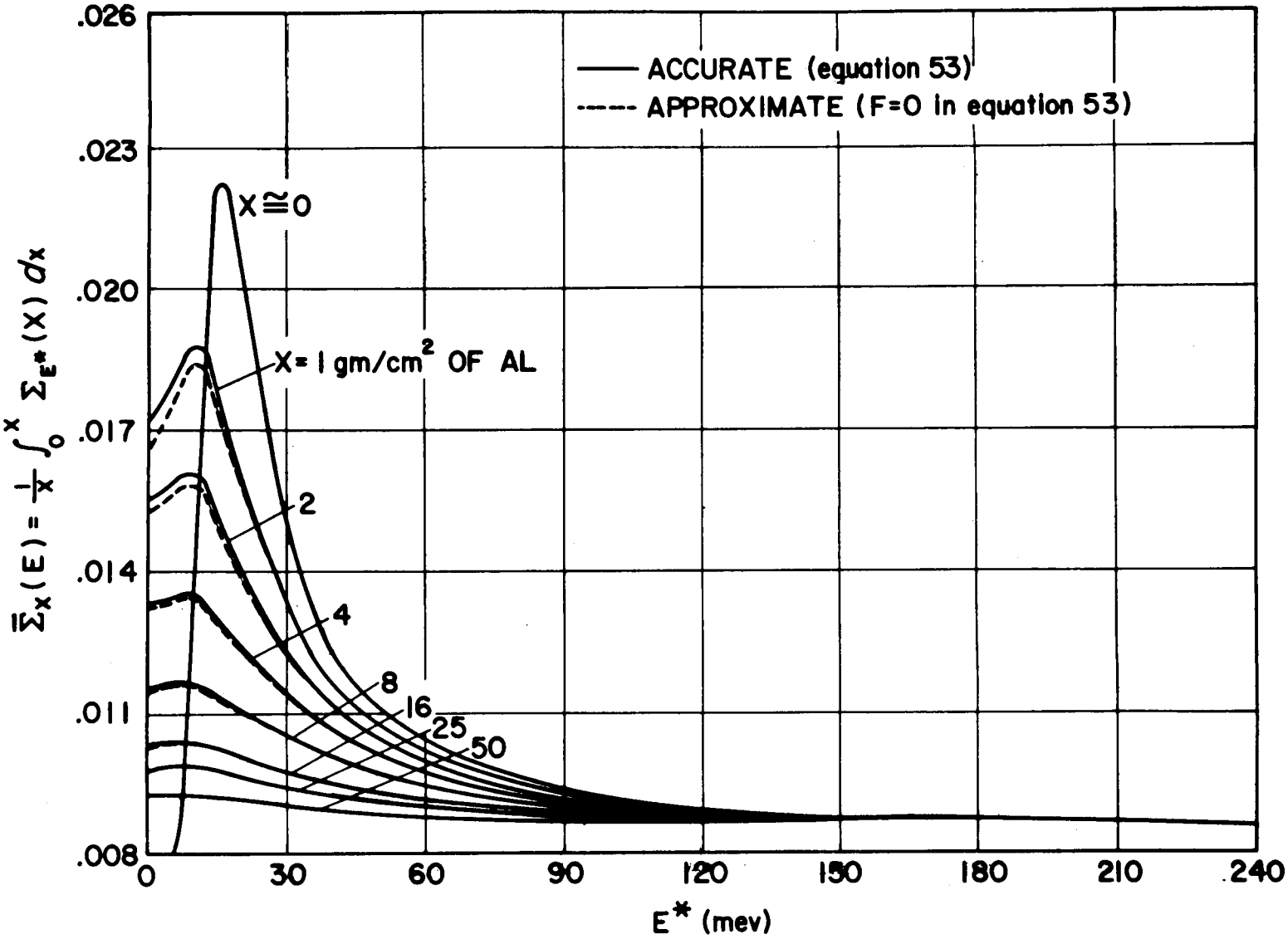

FIGURE 11. AVERAGE PROTON NONELASTIC CROSS SECTION (CM^2/GM) AT DIFFERENT DEPTHS IN ALUMINUM

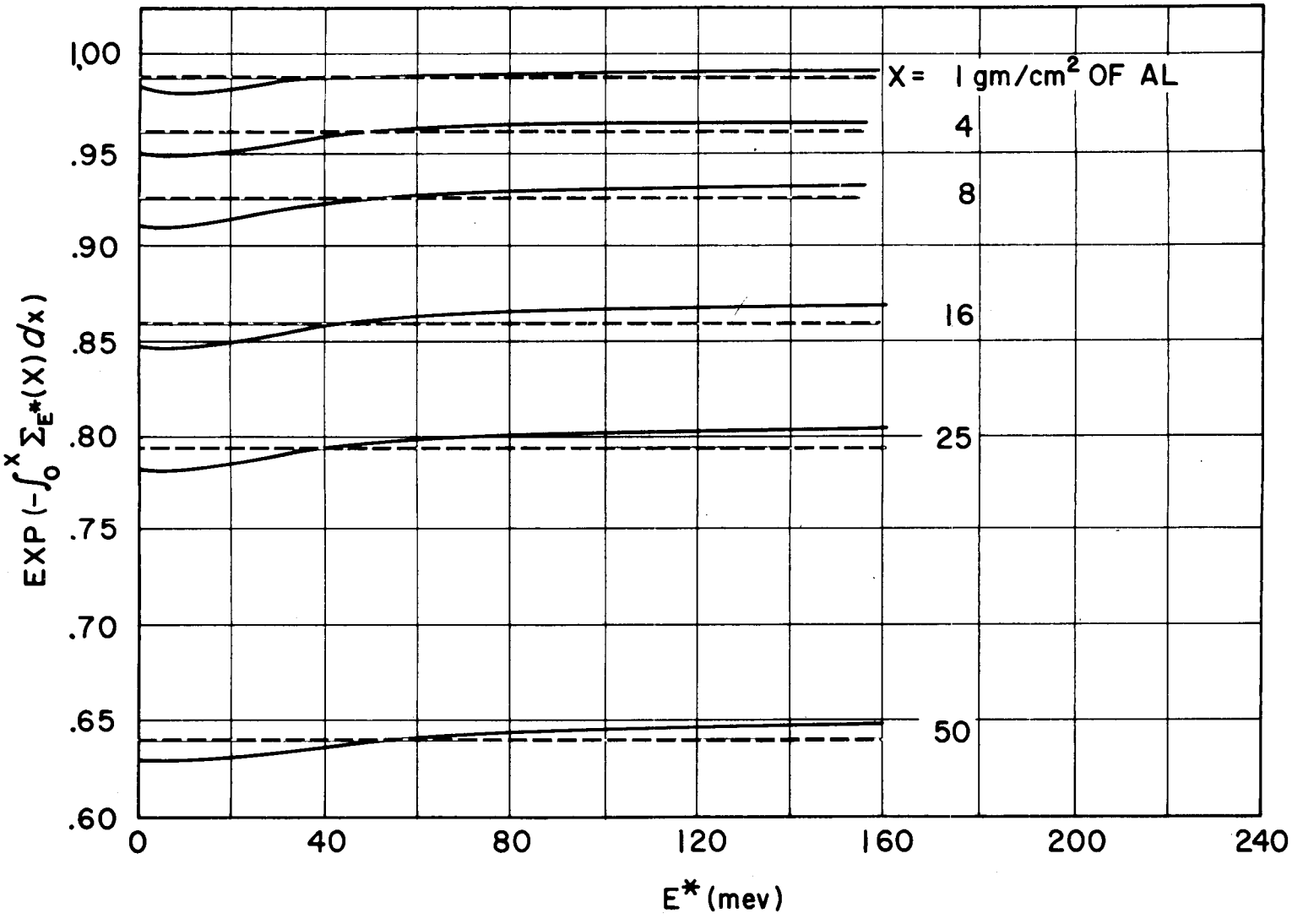

FIGURE 12. ATTENUATION FACTOR OF PROTON FLUX AT DIFFERENT DEPTHS IN ALUMINUM

flux only. In order to estimate the production of secondary particles, Eq. (49) should be used. Thus, the intensity of nonelastic collisions per Mev at energy E^* produced at the depth x is well approximated by the relationship:

$$S_x(E^*) = \sum_{ne}(E^*, A)\ \phi_x(E^*)\ e^{-.009\left(\frac{27}{A}\right)^{.27}x}\left[\frac{\text{collisions}}{\text{gm-Mev}}\right] \quad (61)$$

where the cross section $\sum_n(E^*, A)$ is given by Eq. (49). The energy flux $\phi_x(E^*)$ is given by either Eq. (29) or (30). From Eq. (61), it follows that the total number of nonelastic collisions per gm at depth x is given by

$$S_x = \int_{E^*} S_x(E^*)\, dE^* \left[\frac{\text{collisions}}{\text{gm}}\right] \quad . \quad . \quad (62)$$

However, the results of Eq. (62) are not of importance since the quantities desired are actually the number and energy of secondary neutrons or protons produced at depth x. A further discussion of secondaries will be treated in the next chapter on dose rates. In order to illustrate the nature of the curves depicted by Eq. (61), an incident spectrum of the form

$$N(>p) = N_o e^{-p/p_o}, \quad p > p_1$$

(Eqs. 24 and 30) was chosen. The results of this calculation are shown in Fig. 13. The curve in Fig. 14 illustrates the difference in shape between the flux curve and the nonelastic collision density curve. If a constant cross section was used for $\Sigma_{ne}(E^*, A)$ the curves in Fig. 14 would be exactly parallel.

V. PROTON DOSE RATE CALCULATIONS

The next step in this development is to derive expressions for the primary proton tissue dose or dose rate as a function of shield thickness and/or depth dose in tissue. This is obtained as follows. For the general case after penetrating a depth x in a shield the dose rate is simply given by

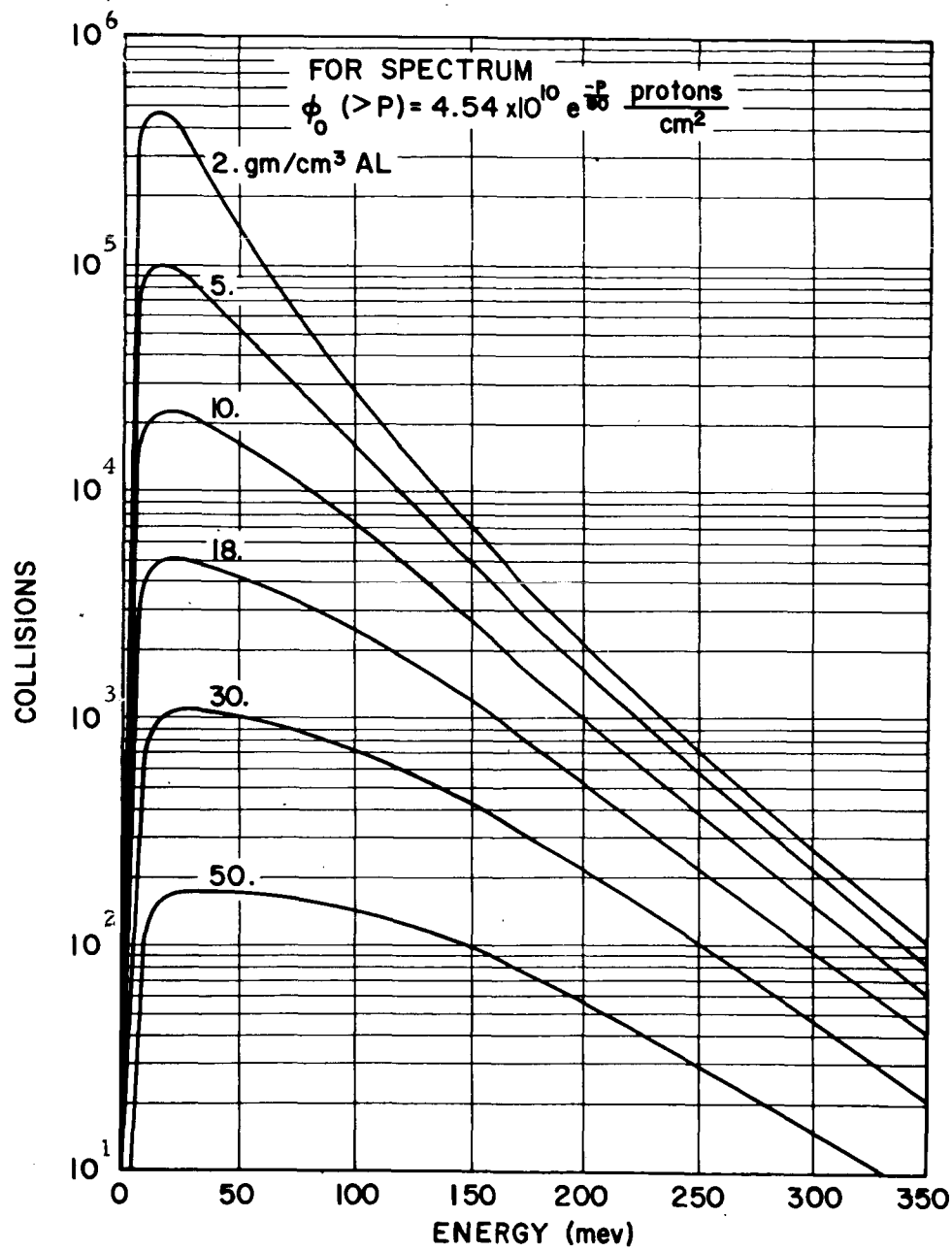

FIGURE 13. NUMBER OF NONELASTIC PROTON COLLISIONS/GM-MEV AS A FUNCTION OF ENERGY AND DEPTH IN ALUMINUM

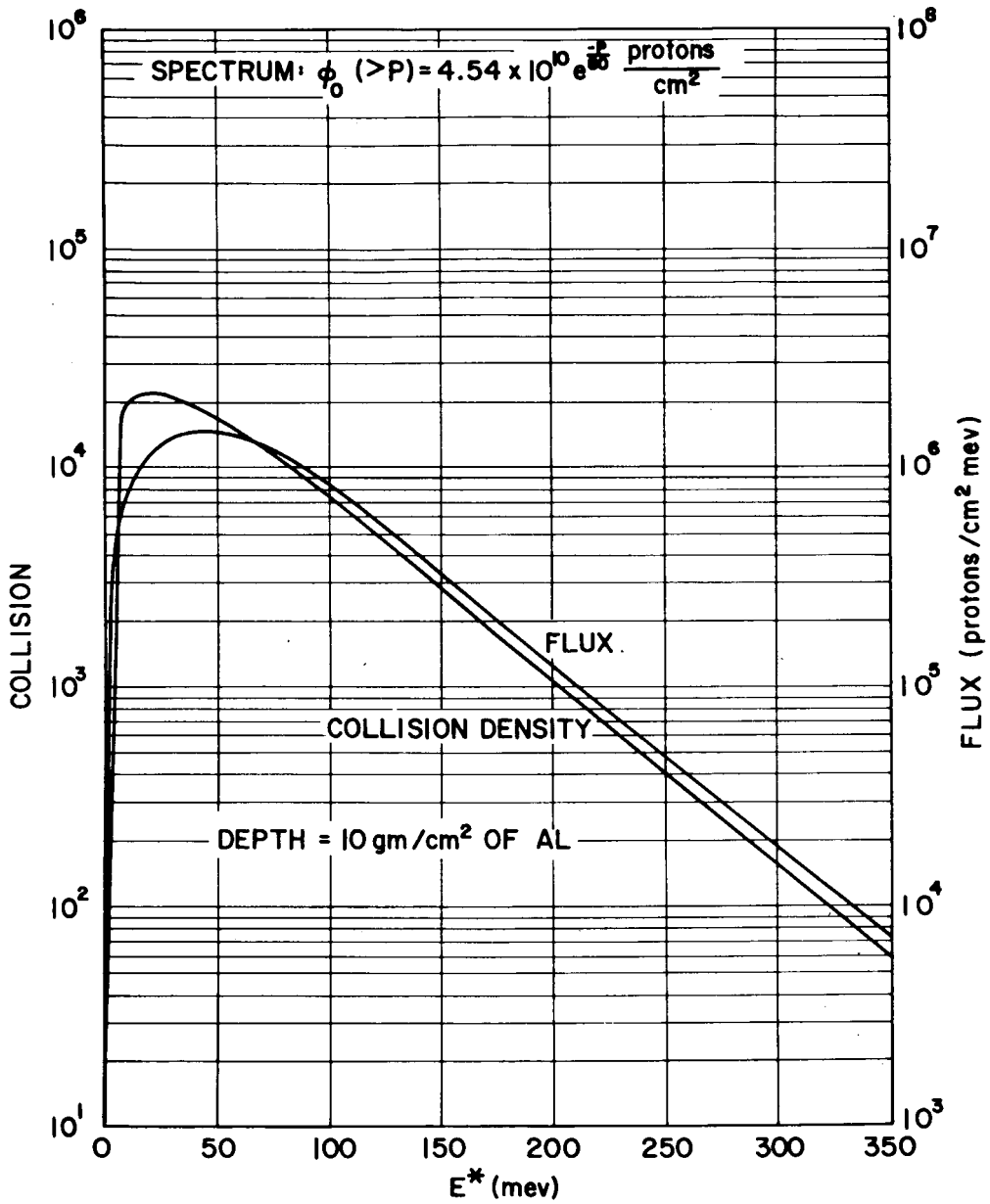

FIGURE 14. COMPARISON OF NONELASTIC PROTON COLLISIONS/GM-MEV TO PROTON DIFFERENTIAL ENERGY SPECTRUM IN 10 GM/CM² OF ALUMINUM

$$D_x = \overline{F} \int_{E_1^*}^{E_2^*} e^{-\int_0^x \Sigma_E(x)\,dx} \phi_x(E^*)\, S(E^*)\, dE^* \qquad (63)$$

where the energy E^* is taken at the penetration depth x. The $S(E^*)$ is the stopping power in tissue and is given by Eq. (1). See Eqs. (57) and (29) or (30) for the first two expressions in the integrand. The $\overline{F}$ is a flux-to-dose conversion factor depending on units of flux. The stopping power formula for tissue can be made compatible with the approximating range equation, (14), in the following manner. Using the definition of Eq. (2), we see that

$$S(E) = -\frac{dE}{dR} = \frac{1}{\frac{d}{dE}\left[\frac{a_o}{2b_o}\log_e(1+2b_o E^{r_o})\right]}$$

or

$$S(E) = \left(\frac{1}{a_o r_o}\right) E^{1-r_o} + \frac{2b_o}{a_o r_o} E \qquad (64)$$

where a_o, b_o, r_o are corresponding range coefficients for tissue (Fig. 15). Using the approximations suggested in the previous chapter for the non-elastic cross sections we can write the proton dose rate after transmitting several layers including tissue in the last layer in the following way:

$$D_x = \overline{F} \int_{E_1^* = \left(\frac{E_1^r - A^*}{B^*}\right)^{1/r} \geq 0}^{E_2^* = \left(\frac{E_2^r - A^*}{B^*}\right)^{1/r}} e^{-(\Sigma_1 X_1 + \Sigma_2 X_2 + \ldots)} \phi(E^*) \left\{\frac{E^{*1-r_o}}{a_o r_o} + \frac{2b_o E^*}{a_o r_o}\right\} dE^* \qquad (65)$$

where

$$\overline{F} = 1.6 \times 10^{-8} \ \frac{\text{rads-cm}^2}{\text{protons}} \quad \text{if} \quad \phi(E^*) \ \text{has units of} \ \frac{\text{protons}}{\text{cm}^2\text{-Mev}},$$

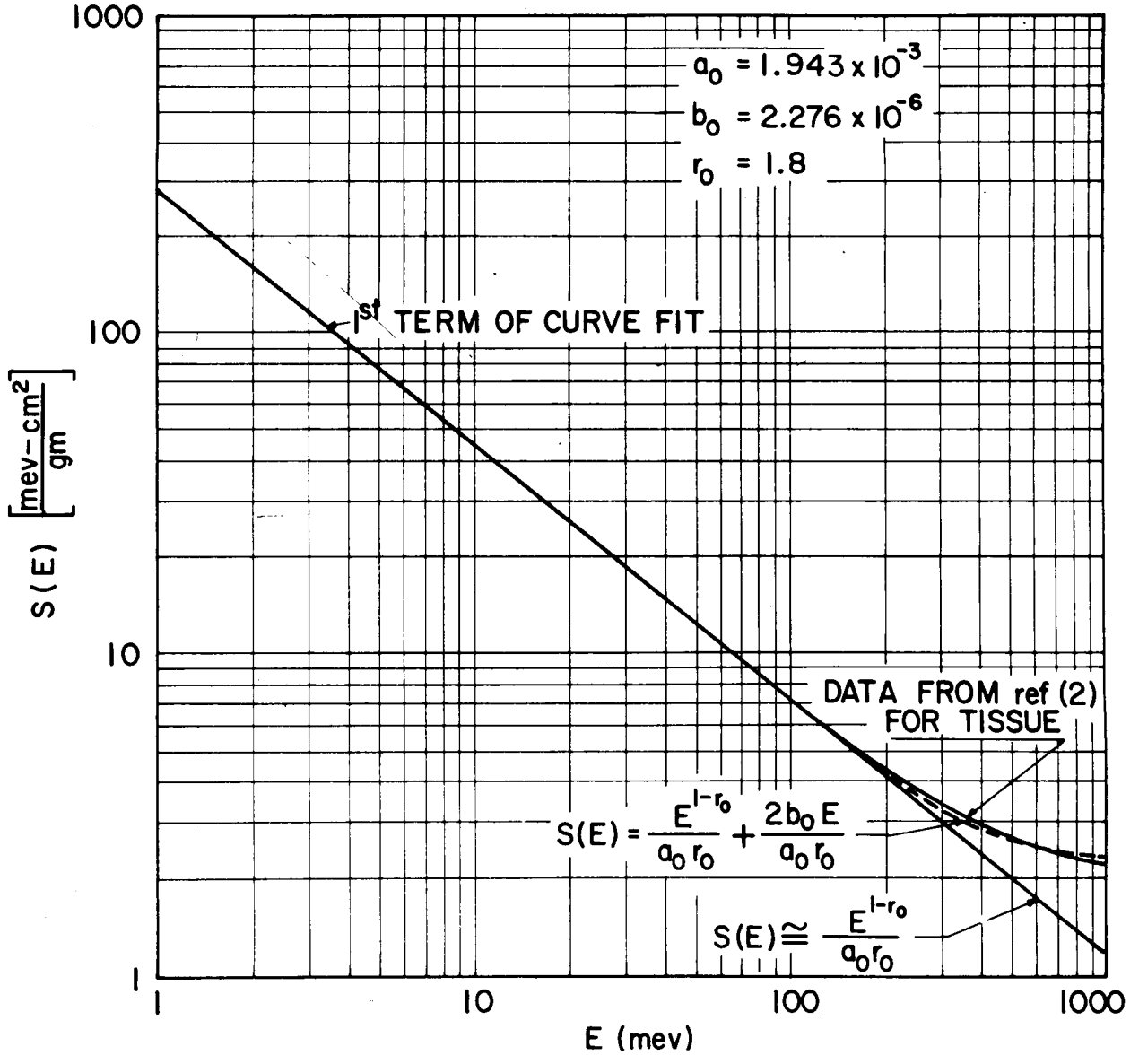

FIGURE 15. STOPPING POWER OF PROTONS IN TISSUE USING APPROXIMATION METHODS

or

$$\bar{F} = 5.76 \times 10^{-5} \ \frac{\text{rads-cm}^2\text{-sec}}{\text{hr-proton}} \quad \text{if } \phi(E^*) \text{ has unit of } \frac{\text{protons}}{\text{cm}^2\text{-sec-Mev}}$$

The flux $\phi(E^*)$ is given by either Eq. (29) or (30) with the constants A^*, B^* defined for multiple layers as shown in Eq. (37). Also it should be noted that the r power used in Eq. (37) is constant for all layers; however, the r_o power used in the stopping power may be different. In fact in all calculations presented in this paper for dose the r is chosen to be 1.78 for the shielding materials, but r_o is 1.80 for the stopping power in tissue. This flexibility permits a small increase in accuracy with little loss in computational speed when numerical integration methods are employed. It should be pointed out that if Eq. (29) is used for the energy flux, then for each energy sector of the spectrum confined between two energies E^*_{i+1} and E^*_i, another integral analogous to Eq. (65), is required, but the integration limits change with the H_i, q_i for each sector. However, this is conveniently carried out in a numerical integration process by using the coefficients H_i, q_i which are necessary to satisfy the limits of Eq. (29) at the energy E^*. Very often it is useful to examine the integrand as a function of E^*. In this manner, a feeling is obtained for the important energy regions in terms of dose. Also, the slope of this curve should indicate the width of energy intervals necessary for an accurate numerical calculation. Thus, the differential proton dose is calculated as follows:

$$\frac{dD_x}{dE} = \bar{F} e^{-(\Sigma_1 X_1 + \Sigma_2 X_2 + \ldots)} \phi(E^*) S(E^*) \ \frac{\text{rads}}{\text{Mev}} \ . \qquad (66)$$

Examples of Eq. (66) are shown in Fig. 16 and 17. The proton dose as a function of depth, calculated from Eq. (65), is shown in Figs. 18 and 19. In the latter two figures, there is a curve labeled "Total Estimated Dose"; this refers to an approximation of dose in rads which corrects for the secondary protons and neutrons generated by nonelastic collisions. The correction is based on the observation that for a shield of low-Z materials the number of secondary protons and neutrons per nonelastic collision at energies below around 200 Mev is less than one cascade particle of each kind (protons and neutrons). With the above observation and other considerations, it became plausible to conjecture that if the nonelastic attenuation factor $\exp(-\Sigma_{ne} X)$ is omitted in the

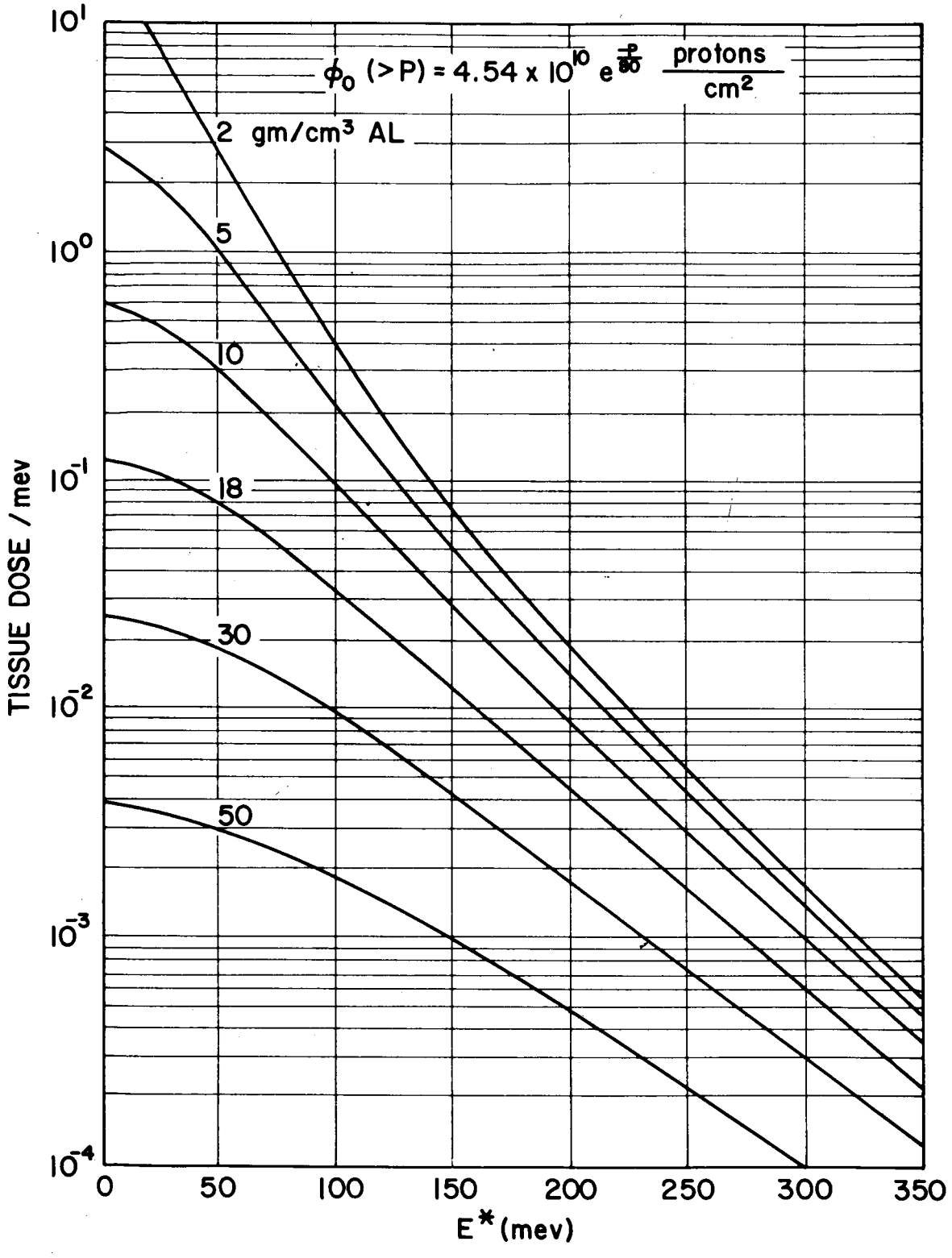

FIGURE 16. DIFFERENTIAL PROTON DOSE IN ALUMINUM

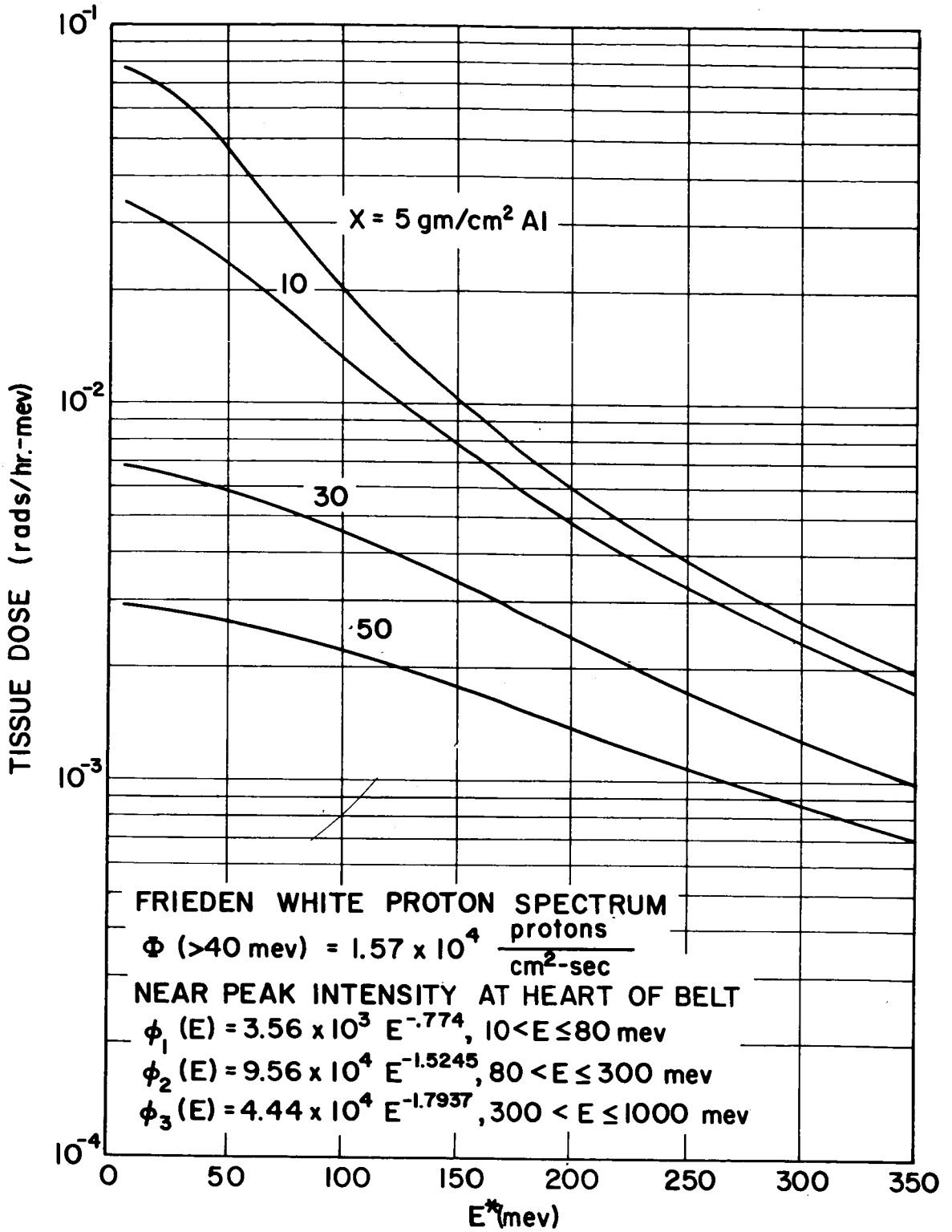

FIGURE 17. DIFFERENTIAL PROTON DOSE IN ALUMINUM

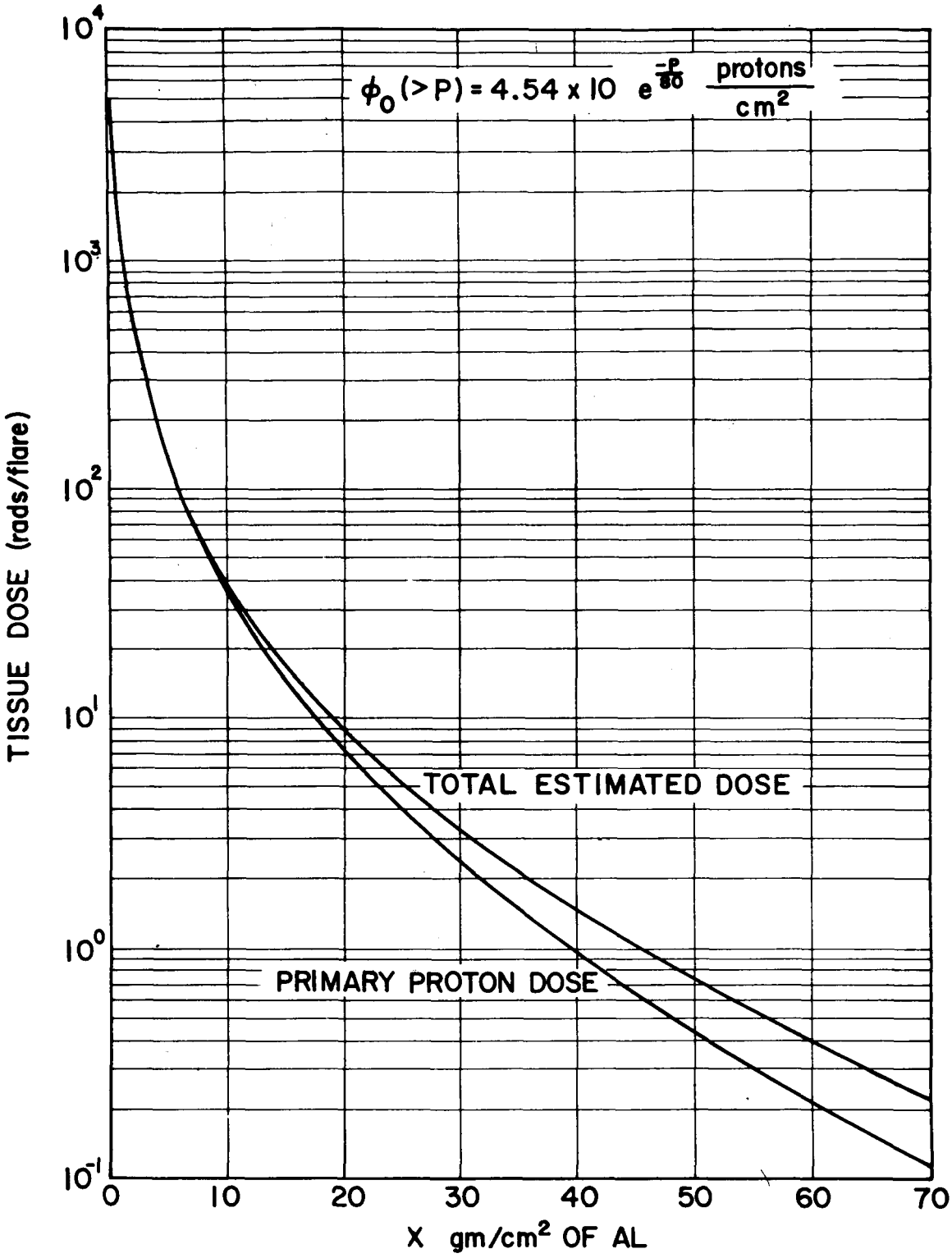

FIGURE 18. PROTON DOSE AT CENTER OF SPHERE

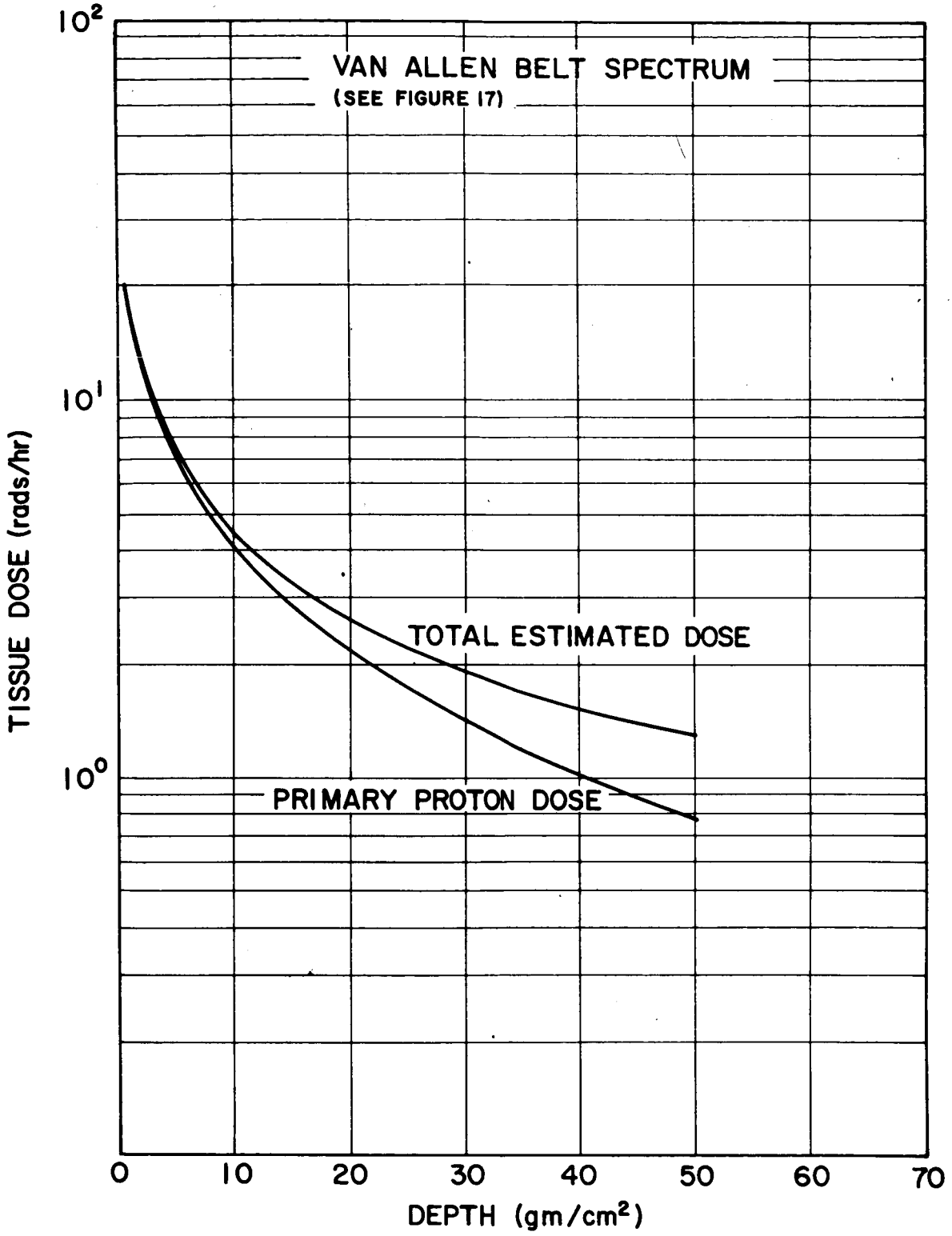

FIGURE 19. PROTON DOSE AT CENTER OF SPHERE

dose calculation, then a correction is made for the secondary particles. The foregoing is the correction made in this paper for the calculations of the "total Estimated Dose." Thus,

$$\text{Total Est. Dose} = \text{Primary Proton Dose} \times \exp\left(\Sigma_1 X_1 + \Sigma_2 X_2 + \ldots\right) \tag{67}$$

Of course such an approximation is only valid within certain fixed limits of shield thickness, Z number of target, and energy of colliding protons. However, to lend validity to the above assumption, Fig. 20 is presented. The secondary data in Fig. 20 were generated by C. W. Hill of Lockheed [2]. The interesting result is that the approximation of Eq. (67) is rather accurate for dose in rads for the thicknesses of aluminum shown. The approximation will probably become less dependable at greater thicknesses, but at these greater depths the total dose is substantially smaller and even a fairly large error in estimating secondary contributions may be unimportant from a practical point of view. Table II provides an analysis of Fig. 20.

The numerical methods used in integrating Eq. (65) consisted simply of the following technique:

$$\int_a^b f(E)\,dE = \Delta \sum_{k=1}^{N} f\left(k\Delta - \frac{\Delta}{2}\right), \tag{68}$$

where

$$\Delta = \frac{b-a}{N} .$$

Since the independent variable (E^*) extends over such a large range, from 0 to over 1000 Mev, the summation of Eq. (68) is carried out in four separate sums so that the Δ can be increased in value as the energies increase. The number of terms in each sum is an input parameter which allows the user of the code to establish his own accuracy.

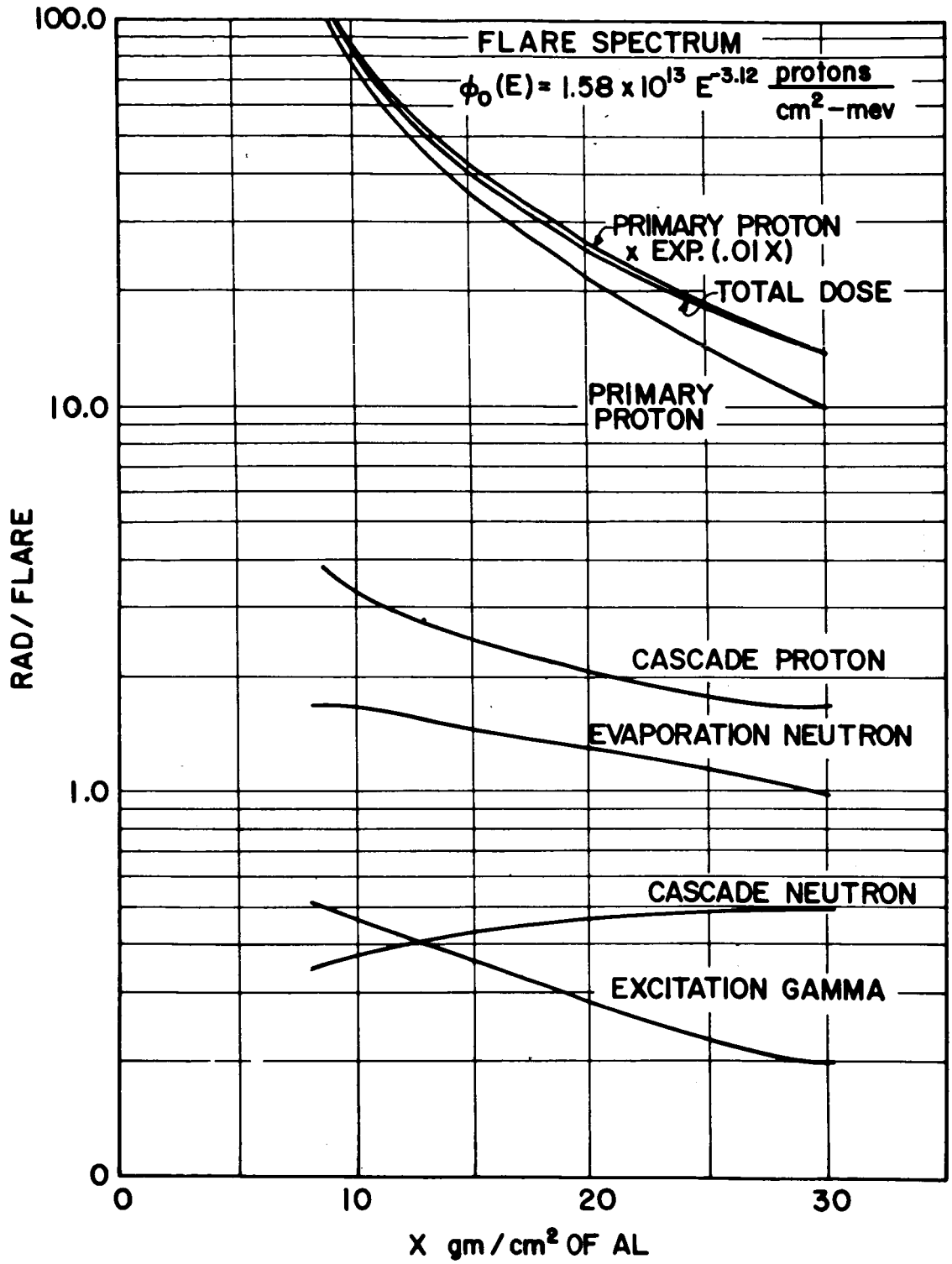

FIGURE 20. COMPARISON OF APPROXIMATION METHOD FOR TOTAL DOSE TO DETAILED CALCULATION OF TOTAL DOSE

TABLE II

Data Analysis

$Z(gm/cm^2)$	Dose of Primary Protons	Total Dose of Secondaries	Total Dose	Primary Dose x exp (.01Z)	% Diff.
10	73.5	5.8	78.8	80.6	2.3
15	36.0	4.7	40.7	41.8	2.7
20	21.5	4.2	25.7	26.2	2.0
25	14.2	3.7	17.9	18.2	1.7
30	10.0	3.4	13.4	13.5	0.75

Some useful simplifications in Eq. (65) can be made if a power law input spectrum (Eq. 29) is used. Thus, the dose rate is represented by

$$D_x = \overline{F} \exp\left[-\Sigma_1 X_1 - \Sigma_2 X_2 - \ldots \right] \int_{\left(\frac{E_i^r - A^*}{B^*}\right)^{1/r}}^{\left(\frac{E_{i+1} - A^*}{B^*}\right)^{1/r}} \frac{H_i B^* E^{*r-1}}{(A^* + B^* E^{*r})^{\frac{r+q_i-1}{r}}} \left(\frac{E^{*1-r_o}}{a_o r_o} + \frac{2 b_o E^*}{a_o r_o} \right) dE^*, \tag{69}$$

where the A^*, B^* are defined for multiple layers in Eq. (37). If we make the change of variables indicated by

$$E^{*r} = \left(\frac{A^*}{B^*}\right)\left(\frac{t}{1-t}\right) \quad \text{or} \quad t = \frac{B^* E^{*r}}{A^* + B^* E^{*r}} \tag{70}$$

and

$$dE^* = \left(\frac{A^*}{B^*}\right)^{1/r} \frac{t^{\frac{1}{r}-1}\, dt}{r(1-t)^{\frac{r+1}{r}}},$$

then, after simplification, we obtain the following:

$$D = \frac{\overline{F} \cdot B^* \exp\left(-\Sigma_1 X_1 - \Sigma_2 X_2 - \ldots\right) H_i}{r A^{*\frac{r+q_i-1}{r}}} \left\{ \frac{1}{a_o r_o} \left(\frac{A^*}{B^*}\right)^{\frac{r-r_o+1}{r}} \int_{1-A^* E_i^{-r}}^{1-A^* E_{i+1}^{-r}} \frac{t^{\frac{1-r_o}{r}}\, dt}{(1-t)^{\frac{r-r_o-q_i+2}{r}}} \right.$$

$$\left. + \frac{2 b_o}{a_o r_o} \left(\frac{A^*}{B^*}\right)^{\frac{r+1}{r}} \int_{1-A^* E_i^{-r}}^{1-A^* E_{i+1}^{-r}} \frac{t^{1/r}\, dt}{(1-t)^{\frac{r-q_i+2}{2}}} \right\}. \tag{71}$$

Now, making the substitutions,

$$m = \frac{1+r-r_o}{r} \quad , \quad n = \frac{r_o+q_i-2}{r}$$

$$m^* = \frac{r+1}{r} \quad , \quad n^* = \frac{q_i - 2}{r} \quad , \tag{72}$$

we obtain, after some additional simplification,

$$D = \frac{\overline{F} \exp(-\Sigma_1 X_1 - \Sigma_2 X_2 - \ldots) H_i}{a_o r_o r A^{*\frac{q-2}{r}} B^{*1/r}} \left\{ \left(\frac{B^*}{A^*} \right)^{\frac{r_o}{r}} \int_{1-A^*E_i^{-r}}^{1-A^*E_{i+1}^{-r}} t^{m-1} (1-t)^{n-1} \, dt \right.$$

$$\left. + 2b_o \int_{1-A^*E_i^{-r}}^{1-A^*E_{i+1}^{-r}} t^{m^*-1} (1-t)^{n^*-1} \, dt \right\}, \tag{73}$$

where the lower limit is set to zero if $A^* \geq E_i^{*r}$. This condition is met when the minimum proton energy E_i has a range equal to or less than the minimum shield thickness. For example, if $E_i = 30$ Mev, then any aluminum thickness greater than 1.175 gm/cm^2 would cause the lower limit to be zero. Thus, one can always choose a thickness of shield so that the integral of Eq. (73) may be written as:

$$D = \phi \left\{ \psi \int_0^{\alpha} t^{m-1} (1-t)^{n-1} \, dt + 2b_o \int_0^{\alpha} t^{m^*-1} (1-t)^{n^*-1} \, dt \right\} . \tag{74}$$

where

$$\phi = \frac{\overline{F} \exp(-\Sigma_1 X_1 - \Sigma_2 X_2 - \ldots) H_i}{a_o r_o r A^{*\frac{q-2}{r}} B^{*1/r}} \quad , \quad \psi = \left(\frac{B^*}{A^*} \right)^{\frac{r_o}{r}} \quad \text{and} \quad \alpha = 1 - A^* E_{i+1}^{-r} .$$

However, the integrals are now recognized as incomplete beta functions. Thus, one may write the dose as simply

$$D = \phi \left\{ \psi \, \beta_{\alpha}(m, n) + 2b_o \, \beta_{\alpha}(m^*, n^*) \right\} . \qquad (75)$$

Now, if the assumption is made that the initial upper energy limit E_{i+1} is sufficiently large, then the value of α approaches 1. Thus, the further simplification in terms of gamma functions is made:

$$D = \phi \left\{ \psi \, \frac{\Gamma(m)\Gamma(n)}{\Gamma(m+n)} + 2b_o \, \frac{\Gamma(m^*)\Gamma(n^*)}{\Gamma(m^*+n^*)} \right\} , \quad q > 2 . \qquad (76)$$

If the stopping power coefficient b_o for tissue is set to zero we get simply:

$$D = \phi\psi \, \frac{\Gamma(m)\,\Gamma(n)}{\Gamma(m+n)} , \quad q > 2 - r . \qquad (77)$$

Equation (77) should be used when $n^* \leq 0$, $(q \leq 2)$. Finally, if all b_i are set to zero for the range coefficients, then $B^*=1$ and $A^* = X_1/a_1 + X_2/a_2 + \ldots$; and if $r_o \equiv r$ we obtain the version of the simplest feasible model for proton dose rate calculations (See Eq. 13.),

$$D = \frac{FH \exp(-\Sigma_1 X_1 - \Sigma_2 X_2 - \ldots)}{a_o r^2 \left(\frac{X_1}{a_1} + \frac{X_2}{a_2} + \ldots \right)^{\frac{r+q-2}{r}}} \; \frac{\Gamma\left(\frac{1}{r}\right)\Gamma\left(\frac{r+q-2}{r}\right)}{\Gamma\left(\frac{r+q-1}{r}\right)} . \qquad (78)$$

The above equations have the defect that the incident proton energy spectrum is represented by only one power function $\phi_o(E) = HE^{-q}$, $E > E_o$ and in Eq. (78) the range is depicted by the simple relation $R = aE^r$. However, the results obtained by using Eq. (76) are quite impressive as is demonstrated in Figs. 21, 22, and 23 by comparison to Alsmiller [5] and Hill [2]. In order to further validate the use of Eq. (76), the comparison of results using Eq. (76) and the same calculation using Eq. (65) with a numerical integration technique given by Eq. (68) is

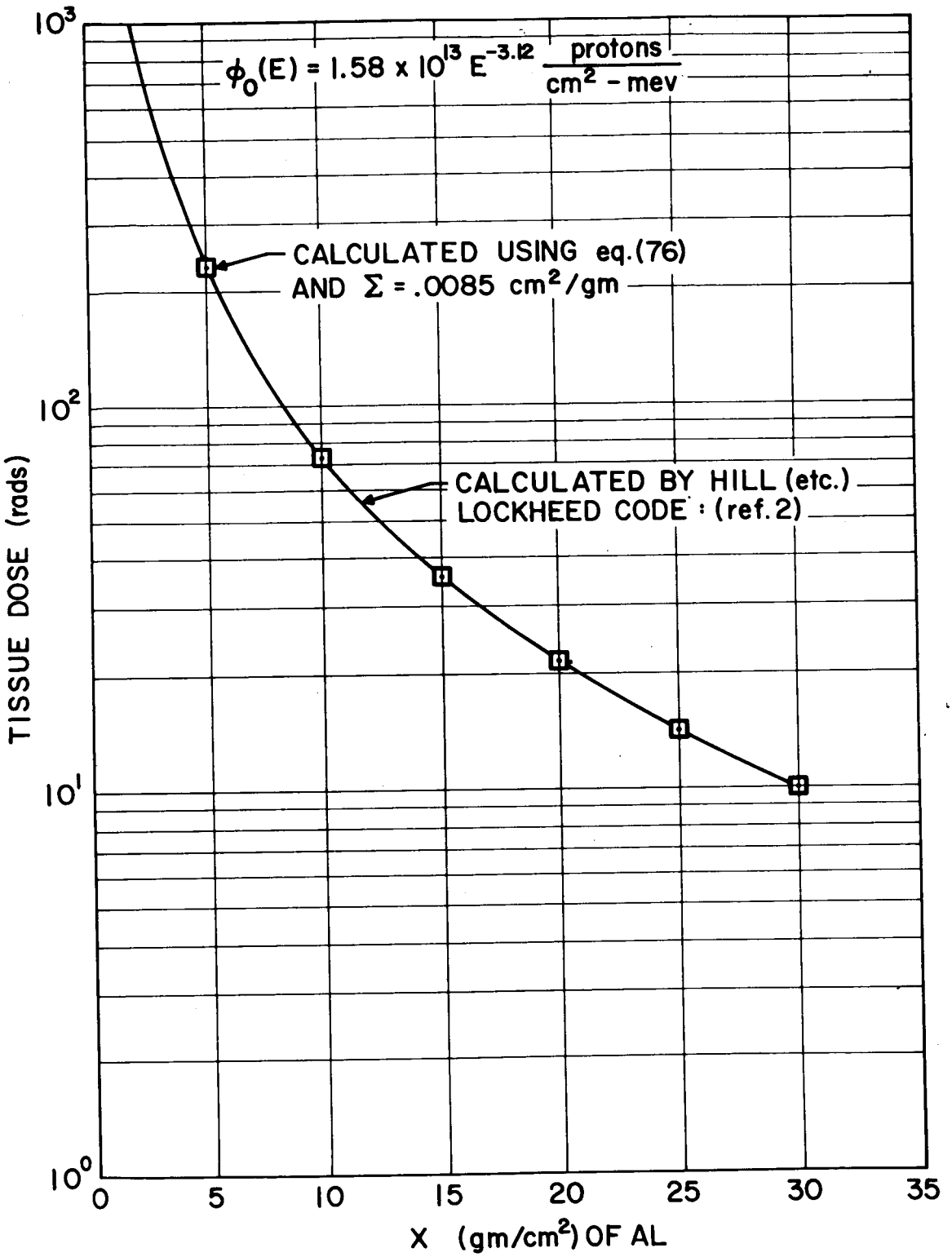

FIGURE 21. COMPARISON OF ANALYTICAL CALCULATION OF DOSE TO NUMERICAL METHODS

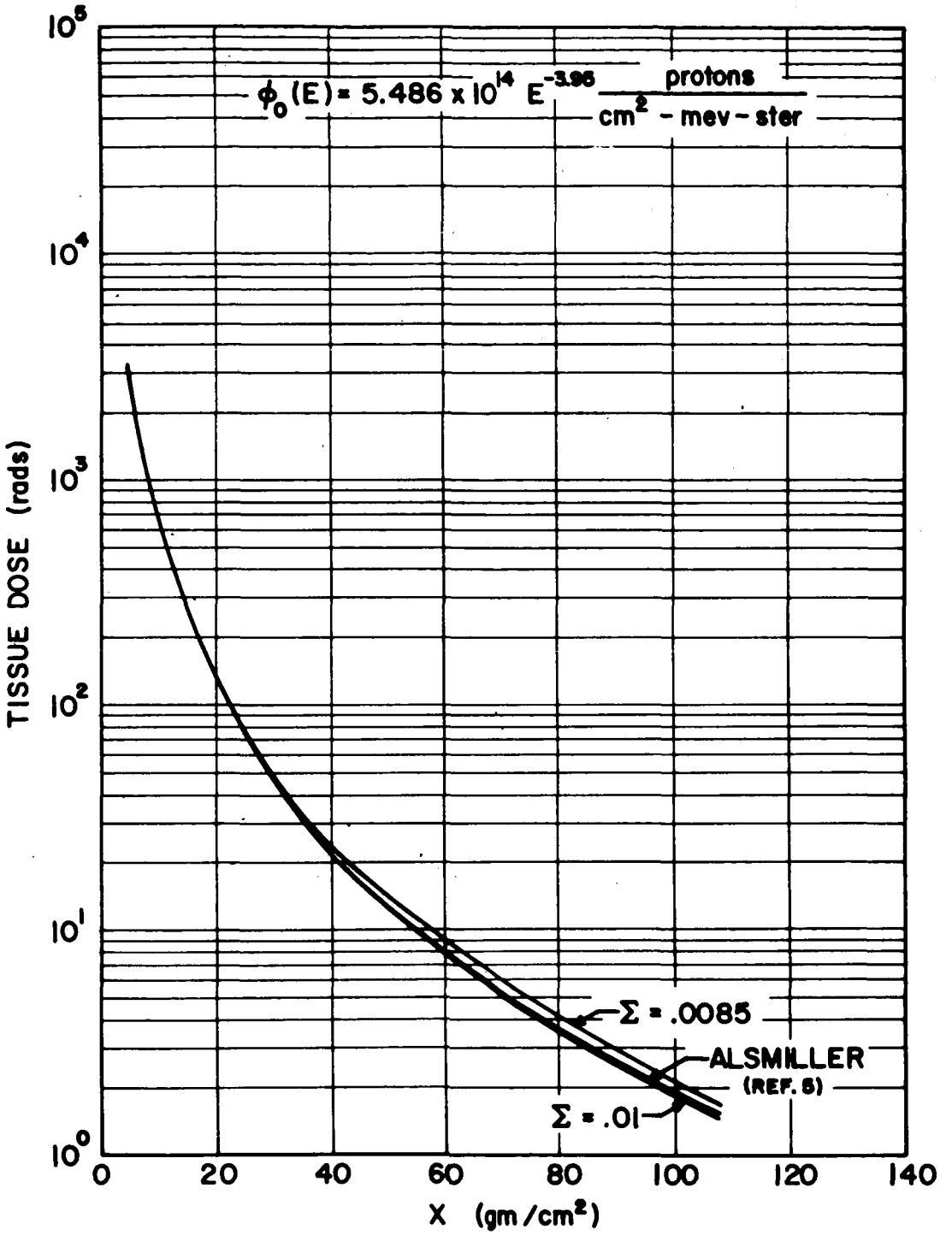

FIGURE 22. COMPARISON OF ANALYTICAL CALCULATION OF DOSE TO NUMERICAL METHODS

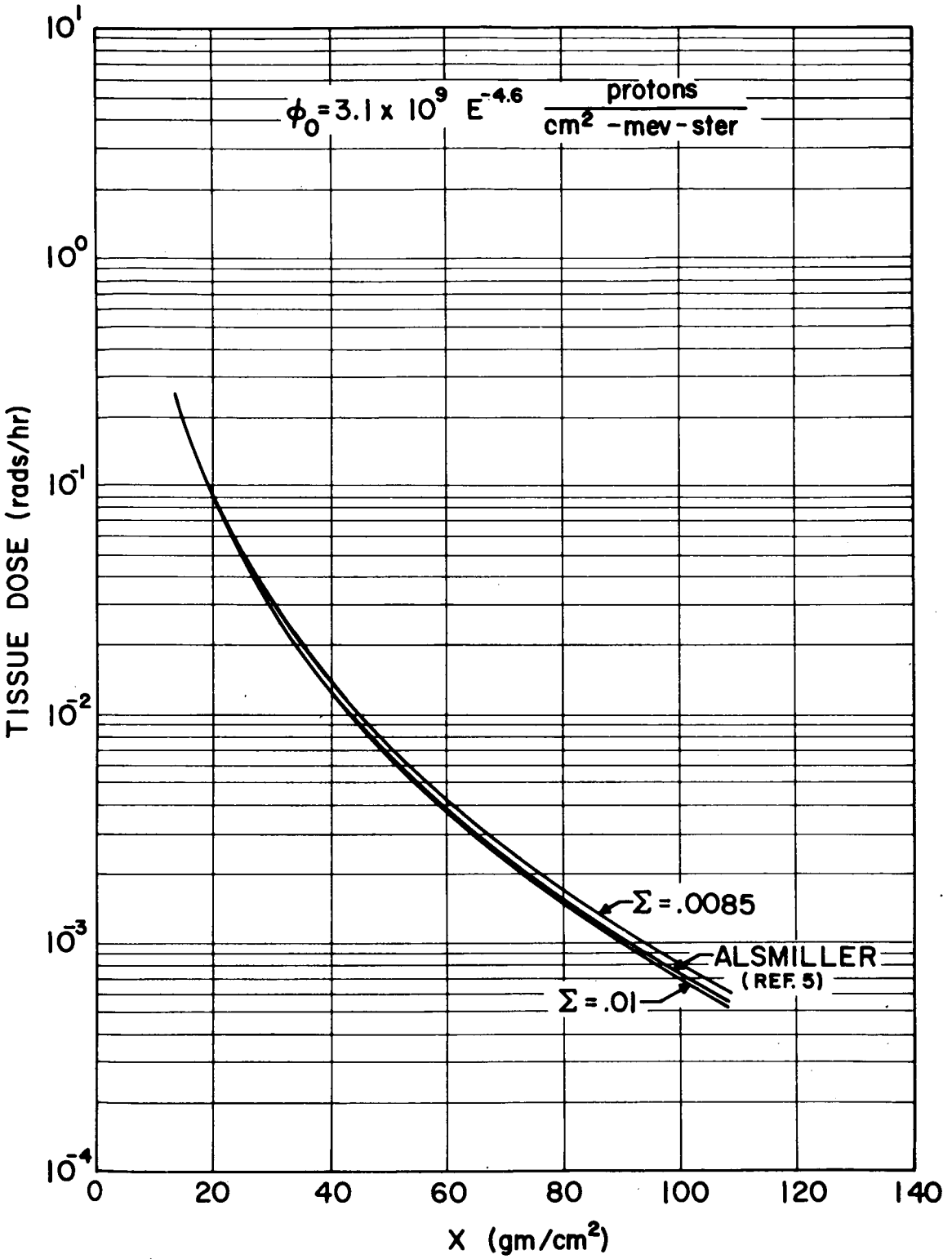

FIGURE 23. COMPARISON OF ANALYTICAL CALCULATION OF DOSE TO NUMERICAL METHODS

made in Fig. 24. Figure 24 depicts the relative error between the gamma function computation (D_Γ) and the numerical method (D_{num}). For a shield thickness less than about 40 gm/cm^2 the D_Γ is about 1/4% higher than the D_{num}. This is probably due to the systematic error introduced in the numerical method which can be improved by taking more terms. (The numerical method used 55 steps between 0 and 1000 Mev.) However, as the thickness increases above 40 gm/cm^2, the relative error increases more rapidly. This is due to two factors. The first is the fact that the gamma function represents an integration from an energy of zero to infinity. The second is the fact that the stopping power formula in tissue (Eq. 64) becomes a very poor approximation above 2000 Mev, resulting in a factor of six over estimation at 10,000 Mev. One solution would be to refit the stopping power formula with more terms so that a more valid approximation is found for energies above 2000 Mev. However, it follows from considerations of the proton differential spectrum that as E^* exceeds 1000 Mev, the proton number approaches zero very rapidly. Hence, the results shown in Fig. 24 imply that even for a thickness of 100 gm/cm^2 of aluminum the relative error due to the poor estimation of stopping power above 2000 Mev results in only a small over-estimate of dose depending fairly strongly on the power of the spectrum. For example, in Fig. 22, with $q = -4.6$ the estimated error at 100 gm/cm^2 due to error in the stopping power above 1000 Mev leads to about a 1/2% over estimate in dose, whereas when $q = -3.95$ this error is about 1%. The remaining differences can be explained by the integration to infinity for the gamma function, and the numerical integration error of about 1/4% in Eq. (65).

The foregoing analysis gave an indication of the numerical errors which occur in the proton dose rate calculation. However, a very important source of error is often ignored in such discussions. What happens if the range energy data is systematically in error by some small amount? Analysis by the author has found that, in general, if the range is consistently low or high by, say, x%, then the dose is consistently low or high by about 2x%. Thus a systematic error in range is reflected twice as great in the dose calculation. An example of the foregoing is presented in Fig. 25, and a detail error analysis of this figure and two other systematic errors are shown in Table III.

The results of Table III, however, have one consoling aspect and this is that the errors are approximately uniformly displaced from

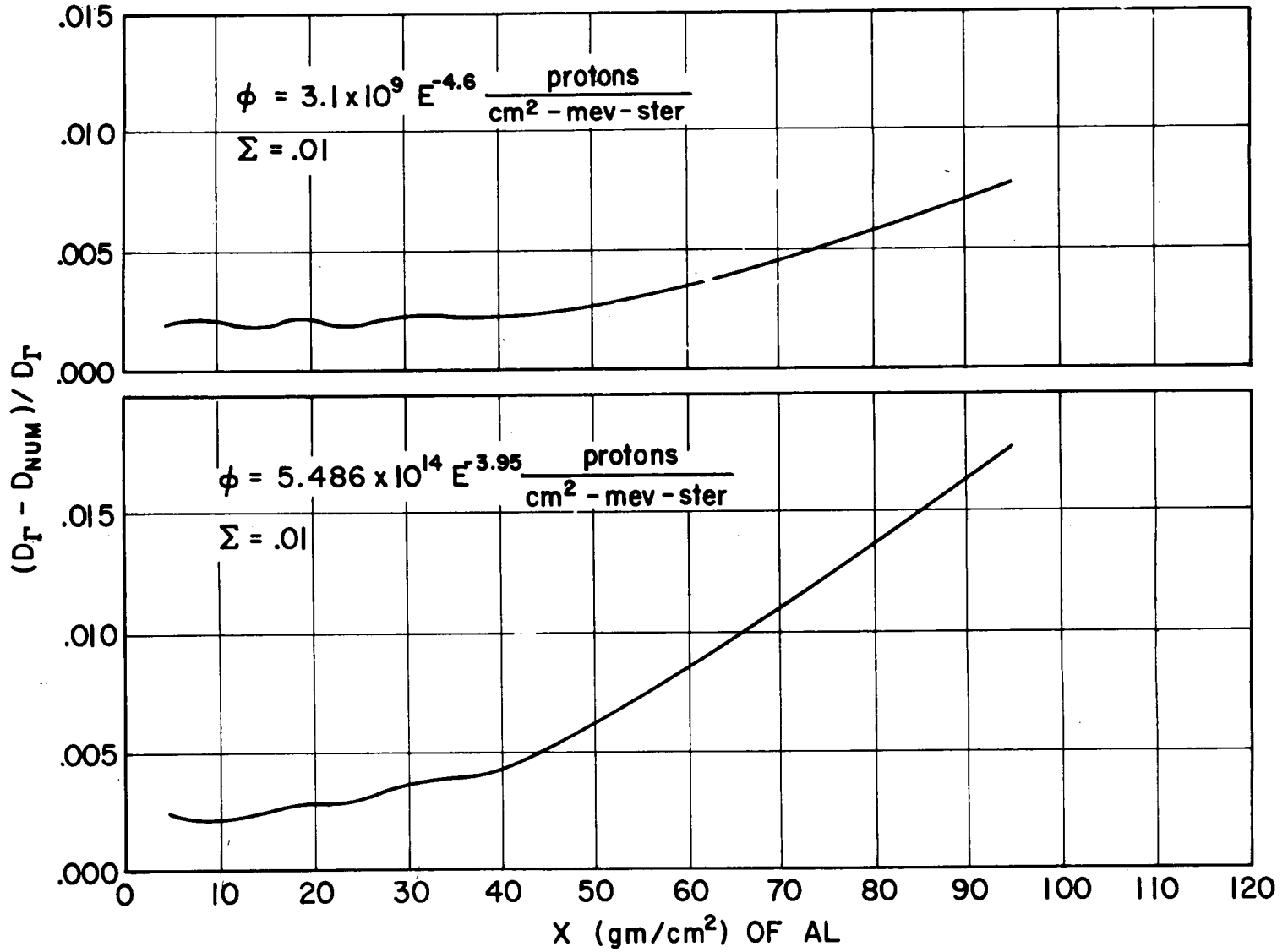

FIGURE 24. RELATIVE DIFFERENCE BETWEEN NUMERICAL INTEGRAL OF DOSE AND ANALYTICAL APPROXIMATION

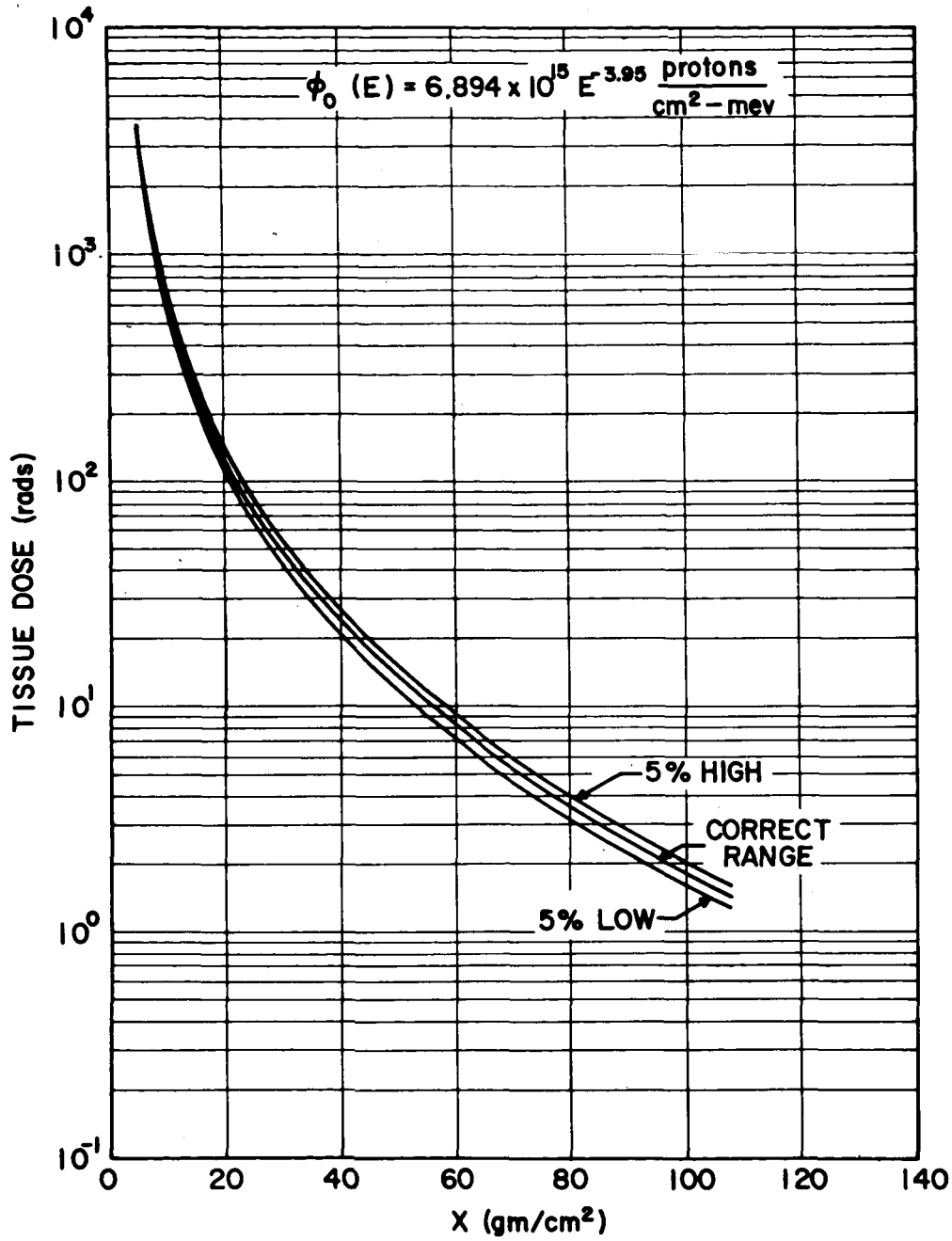

FIGURE 25. EFFECT ON DOSE RATE AT CENTER OF SPHERE WHEN SYSTEMATIC ERROR OF 5% IS MADE IN PROTON RANGE

TABLE III

Comparison of Relative Errors in Primary Proton Dose
Where the Proton Range Has Been
Systematically Under- or Over-Estimated

gm/cm^2	Dose* for Accurate Range	Relative Error for +5%**	Relative Error for -5%	Relative Error for +10%	Relative Error for -10%	Relative Error for +15%	Relative Error for -15%
4.5	3.331×10^3	+.1010	-.1104	+.2225	-.1988	+.3425	-.2900
9.0	7.387×10^2	+.1010	-.1105	+.2225	-.1988	+.3427	-.2901
18.0	1.564×10^2	+.1012	-.1106	+.2228	-.1991	+.3430	-.2905
27.0	6.072×10^1	+.1013	-.1107	+.2231	-.1993	+.3435	-.2907
54.0	1.068×10^1	+.1018	-.1112	+.2242	-.2000	+.3452	-.2922
81.0	3.437×10^0	+.1026	-.1119	+.2258	-.2016	+.3476	-.2939
108.0	1.415×10^0	+.1035	-.1127	+.2276	-.2031	+.3505	-.2962

* Rads at center of sphere; $\phi_o(E) = 6.894 \times 10^{15} E^{-3.95}$ protons/cm^2 Mev.

** Relative error in dose when range is 5% too high but the stopping power in tissue is correct.

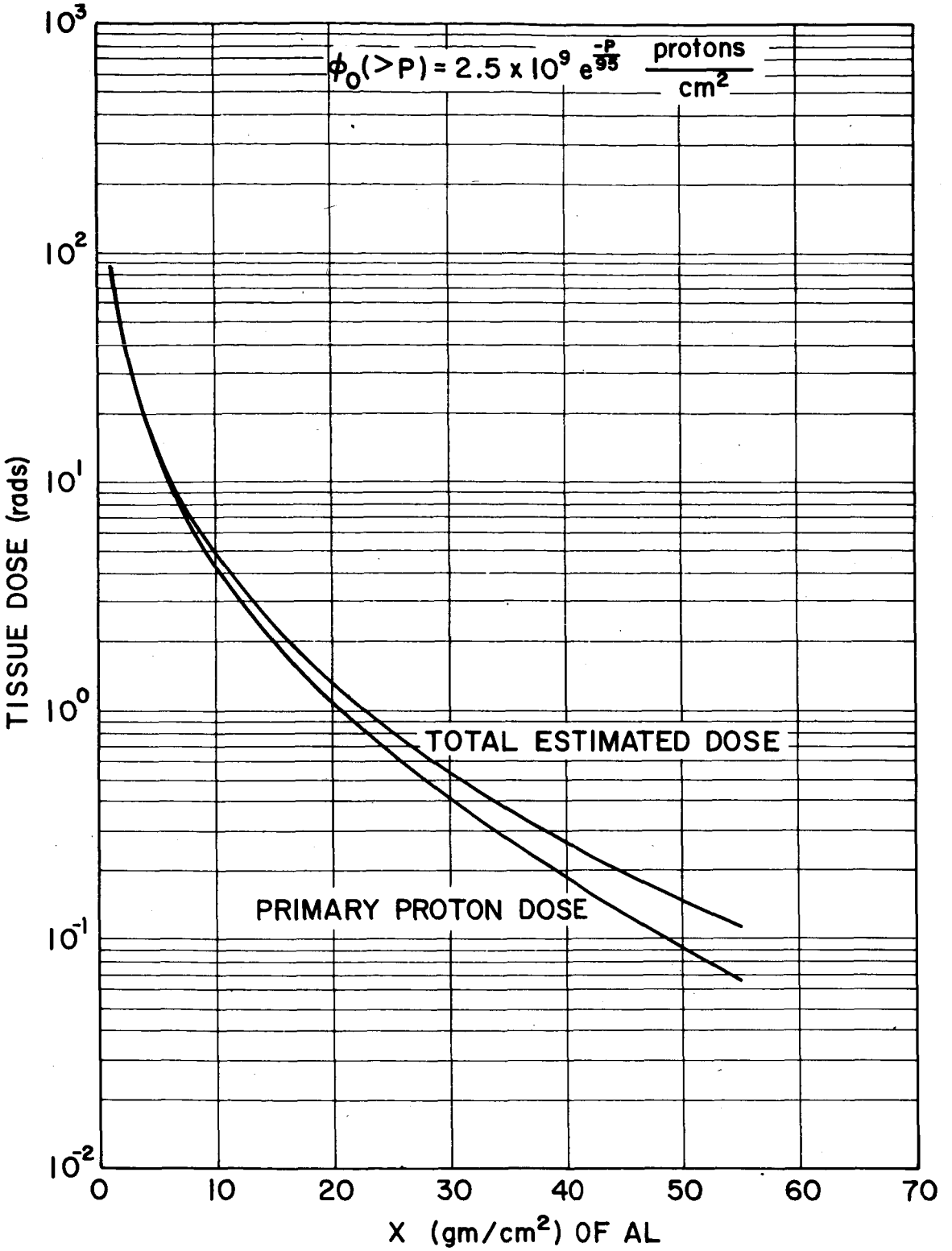

FIGURE 26. DOSE RATE AT CENTER OF SPHERE FROM A TYPICAL FLARE

the correct calculations. Thus one hopes that the deviations of the Bethe-Bloch range energy calculations vary randomly from the true proton range so that the error is periodic from say +5% to -5% and oscillating several times between 10 Mev and 1000 Mev, then the above type error in the dose calculation might well approach zero.

As a final presentation in this section on Proton Dose Rates, a cursory analysis was made of solar proton events presented in Ref.[6] by W.R. Webber of the University of Minnesota. The result was a pseudo-average flare based on data from 1956 through 1962. This flare is represented by the integral rigidity spectrum

$$N(>p) = 2.5 \times 10^9 \quad e^{-\frac{p}{95}} \left[\frac{\text{protons}}{\text{cm}^2\text{-flare}}\right] , \qquad (79)$$

where p is in units of MV (million volts), Rather interesting is the fact that even though the above flare is sort of an average, the probability is only 0.025 that a more intense flare occurred during any one-week period between 1956 and 1962. Thus one could assume that the above flare represents a model for proton flares per week with a .975 probability that the calculated doses will not be exceeded. The dose rates for the above spectrum at the center of a spherical enclosure of variable aluminum thicknesses is presented in Fig. 26.

VI. ISOTROPIC INCIDENT PROTON FLUX ON SLABS

In the foregoing the calculations were for normal incident protons on plane slabs. Even though the calculations are denoted as dose rates at the center of spheres the computational geometry is for a monodirectional normal incident flux. If one wishes to extend the above calculations to oblique incidence, the only change necessary is that the slab layers X_i be replaced by the thickness along the slant path of the oblique proton flux. Thus, the slant thickness is simply

$$\rho_i = X_i/\cos \theta_o , \qquad (80)$$

where θ_o is the angle between the slab normal and the angle of incidence of the proton flux. Thus it would be fairly simple, for any incident angular distribution, to calculate the dose rate at a given depth by calculating the proper solid angle weighting function and employing only the dose rate data for normal incidence. Thus, for the isotropic incident case one sees that if the normal incident dose, $D(X_i)$, is calculated for the omnidirectional flux, then the primary proton dose rate for the isotropic incident flux on a slab is given by

$$D_{Iso.} = 2\pi \int_0^1 \frac{1}{4\pi} D\left(\frac{X}{\cos\theta}\right) d\cos\theta \,, \tag{81}$$

or numerically the simple summation

$$D_{Iso.} = \frac{1}{2N} \sum_{i=1}^{N} D_i\left(\frac{X_i}{\cos\theta_i}\right) \,, \tag{82}$$

where

$$\cos\theta_i = \frac{1}{N}\left(i - \tfrac{1}{2}\right) .$$

The above increment in $\cos\theta$ represents taking the i^{th} dose component at the midpoint of the i^{th} solid angle. Also, the use of Eq. (82) would embody utilizing interpolation in a precalculated table of dose as a function of thickness. The above method was not utilized in the foregoing calculations even though it merits consideration as a computational method. The dose for an isotropic incident proton flux on a slab was calculated by employing numerical integration on the double integral below:

$$D_{Iso.} = 2\pi F \int_{E_1^*}^{E_2^*} \int_0^{\pi/2} e^{-\bar{\Sigma}_{ne}\rho} \phi_\rho(E^*)\, S(E^*) \sin\theta \, d\theta \, dE^* \,, \tag{83}$$

where the $\rho = X/\cos\theta$ and the calculations of B^*, A^* (Fig. 7) are calculated using $\rho_i = X_i/\cos\theta_i$ for the slab penetration thicknesses. The results of the isotropic incident proton slab calculations are presented in Figs. 27 through 32. In Fig. 27, a comparison is made with Alsmiller's

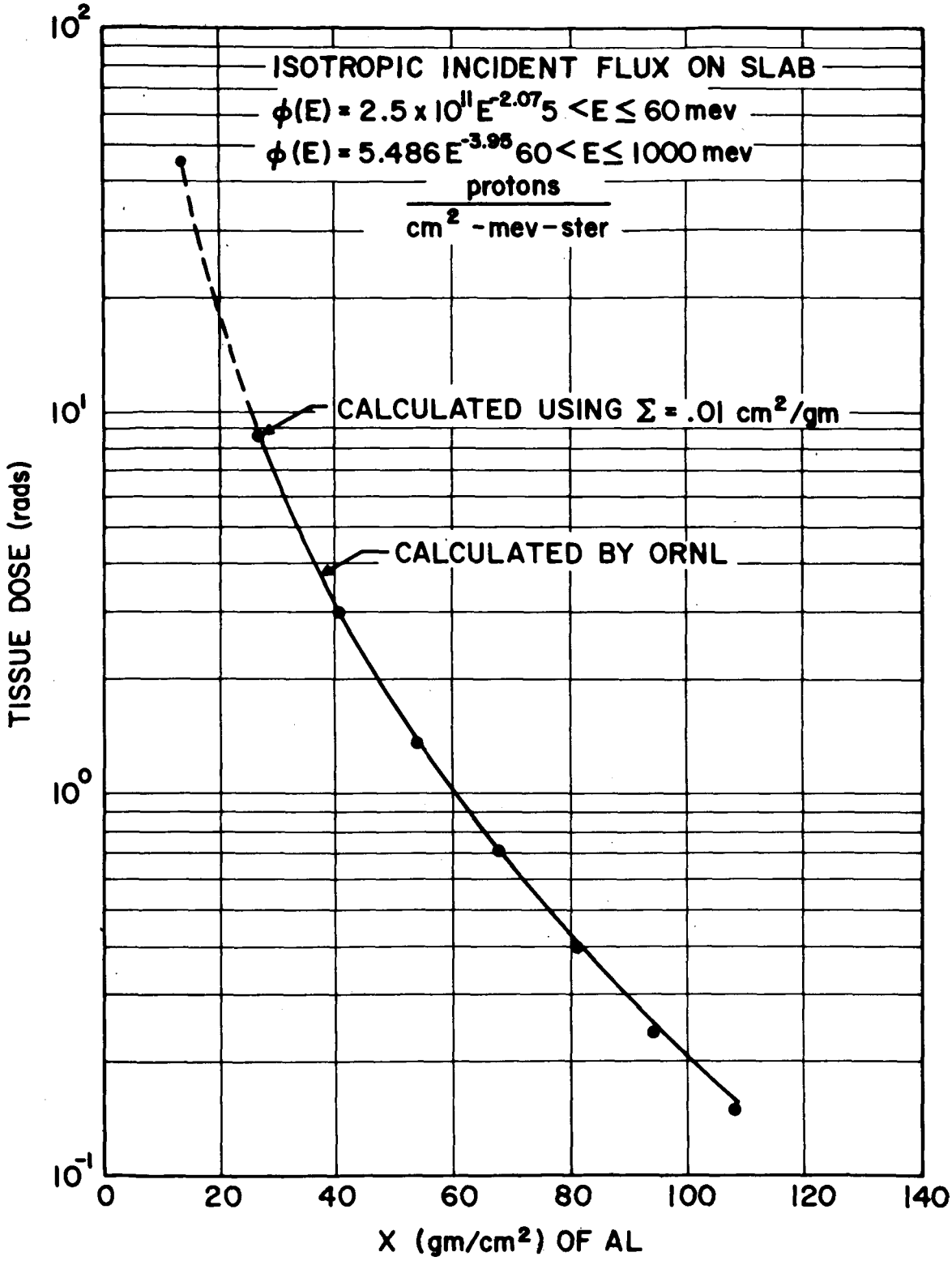

FIGURE 27. SLAB PROTON DOSE RATE FROM ISOTROPIC INCIDENT FLUX COMPARED TO ALSMILLER [5]

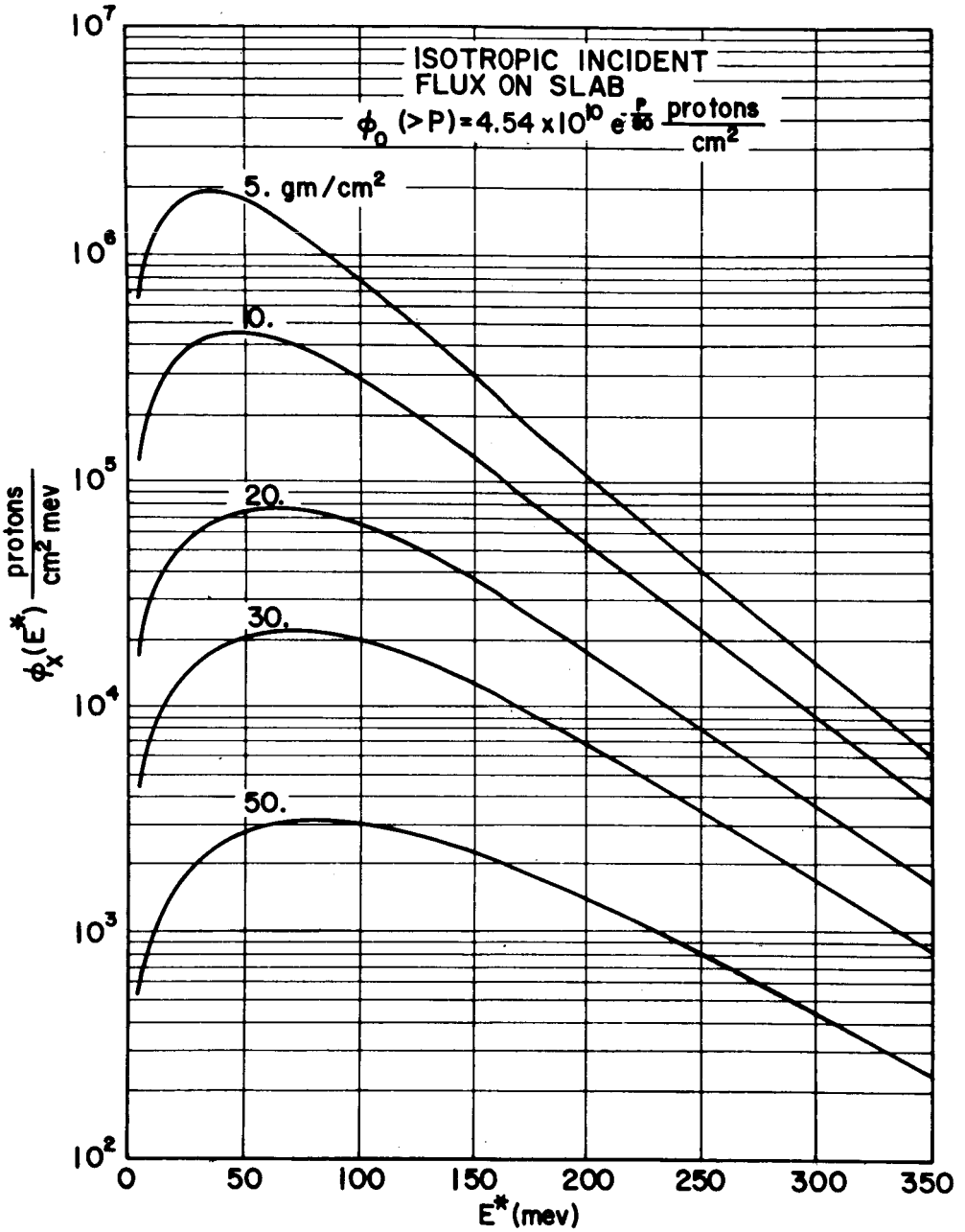

FIGURE 28. DIFFERENTIAL PROTON ENERGY SPECTRUM AT DIFFERENT DEPTHS IN ALUMINUM FOR ISOTROPIC INCIDENT FLUX ON SLAB

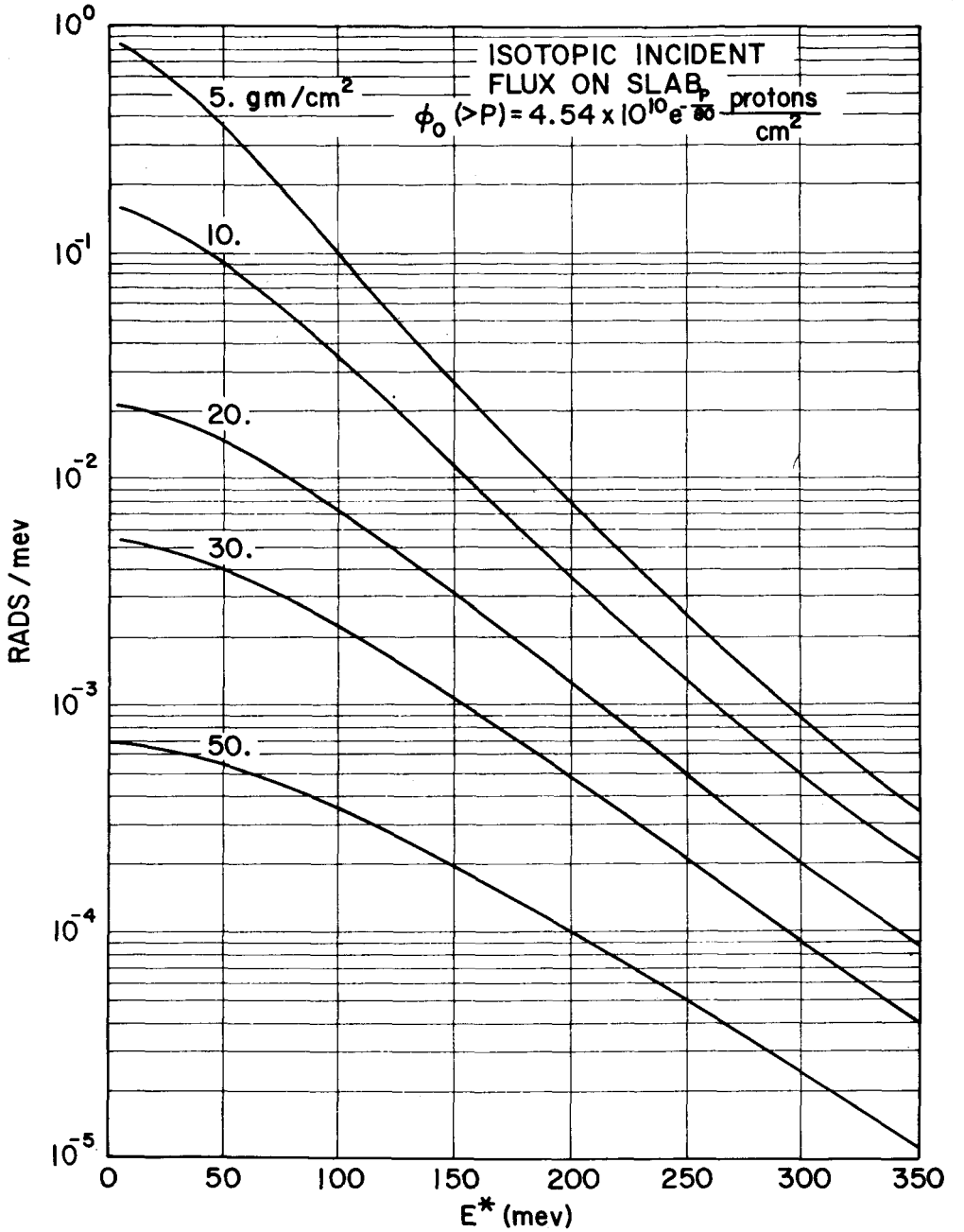

FIGURE 29. DIFFERENT PROTON DOSE AT DIFFERENT DEPTHS IN ALUMINUM FOR ISOTROPIC INCIDENT FLUX ON SLAB

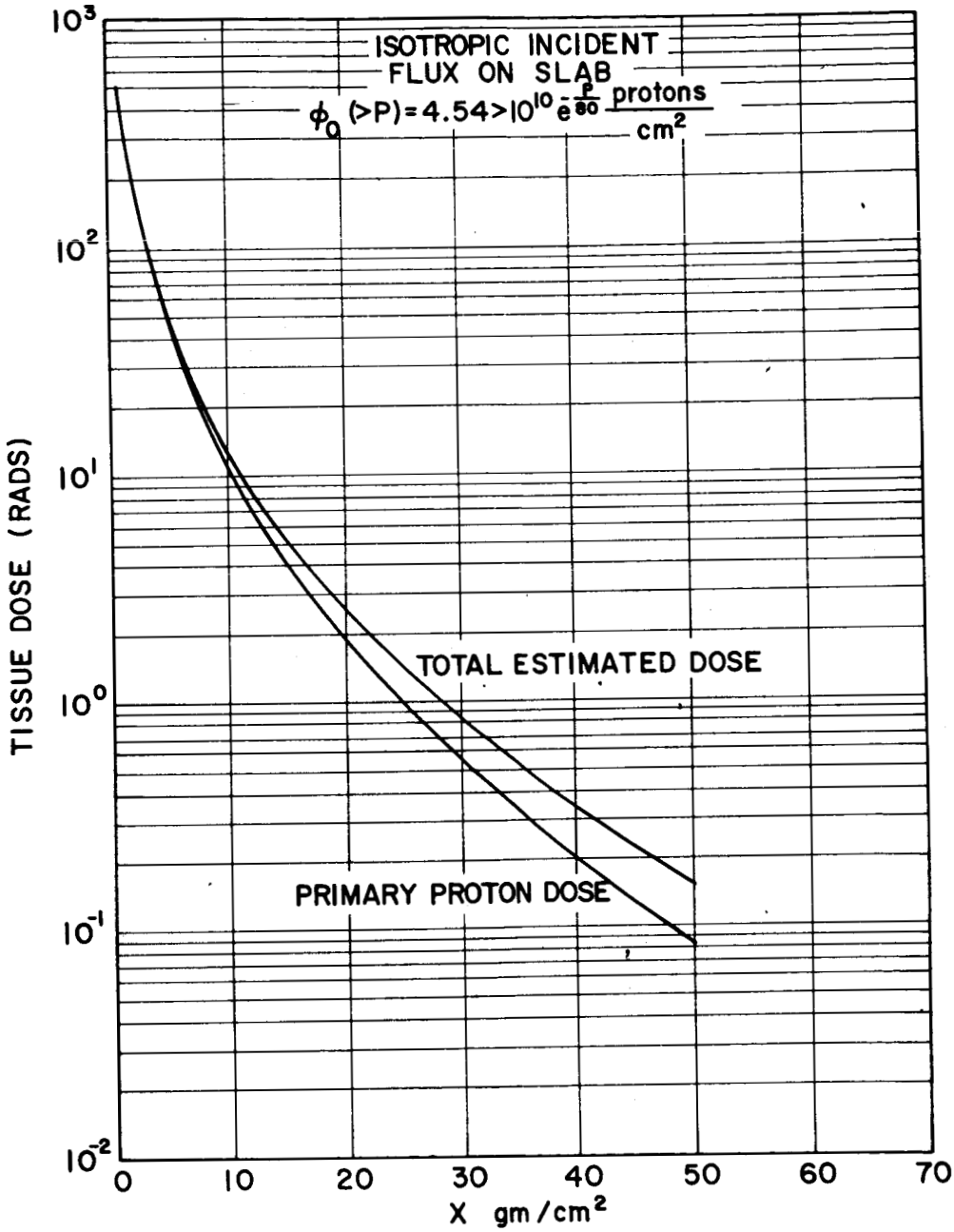

FIGURE 30. PROTON DOSE AS FUNCTION OF SLAB THICKNESS FOR ISOTROPIC INCIDENT FLUX ON SLAB

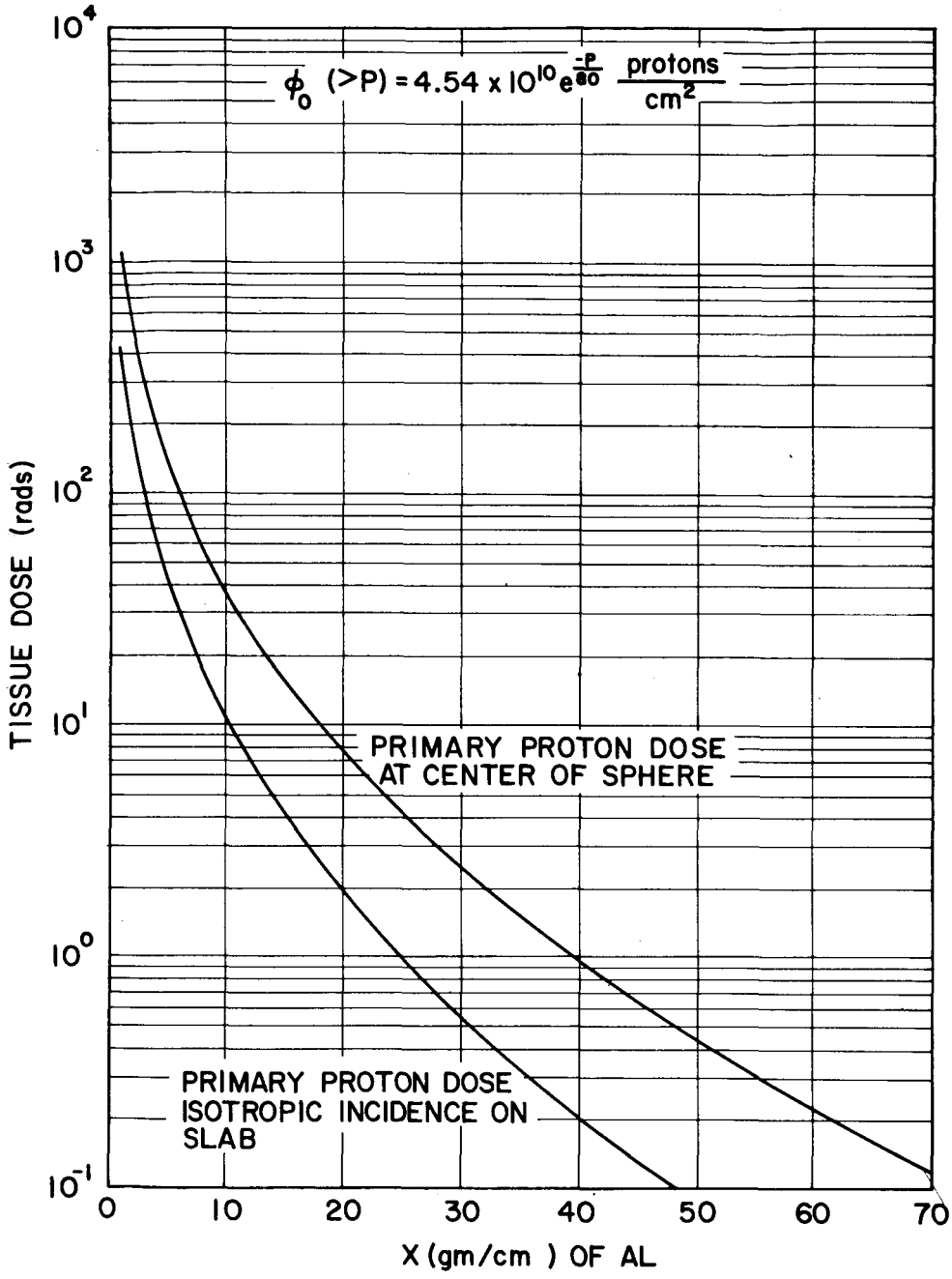

FIGURE 31. COMPARISON OF DOSE FOR ISOTROPIC INCIDENT FLUX ON SLAB AND DOSE AT CENTER OF SPHERE

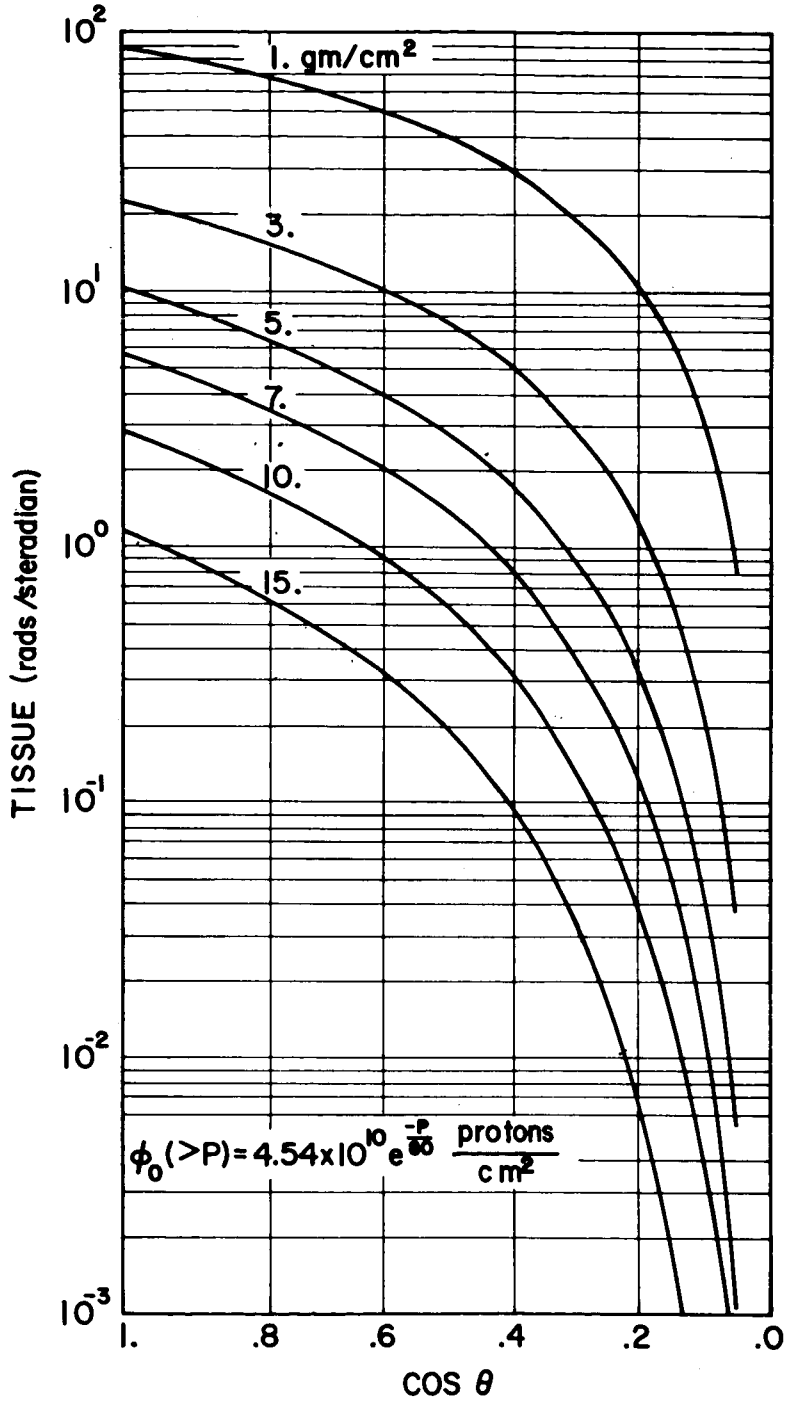

FIGURE 32. PROTON DOSE PER STERADIAN FOR ISOTROPIC INCIDENT FLUX ON SLAB OF ALUMINUM AT DIFFERENT DEPTHS

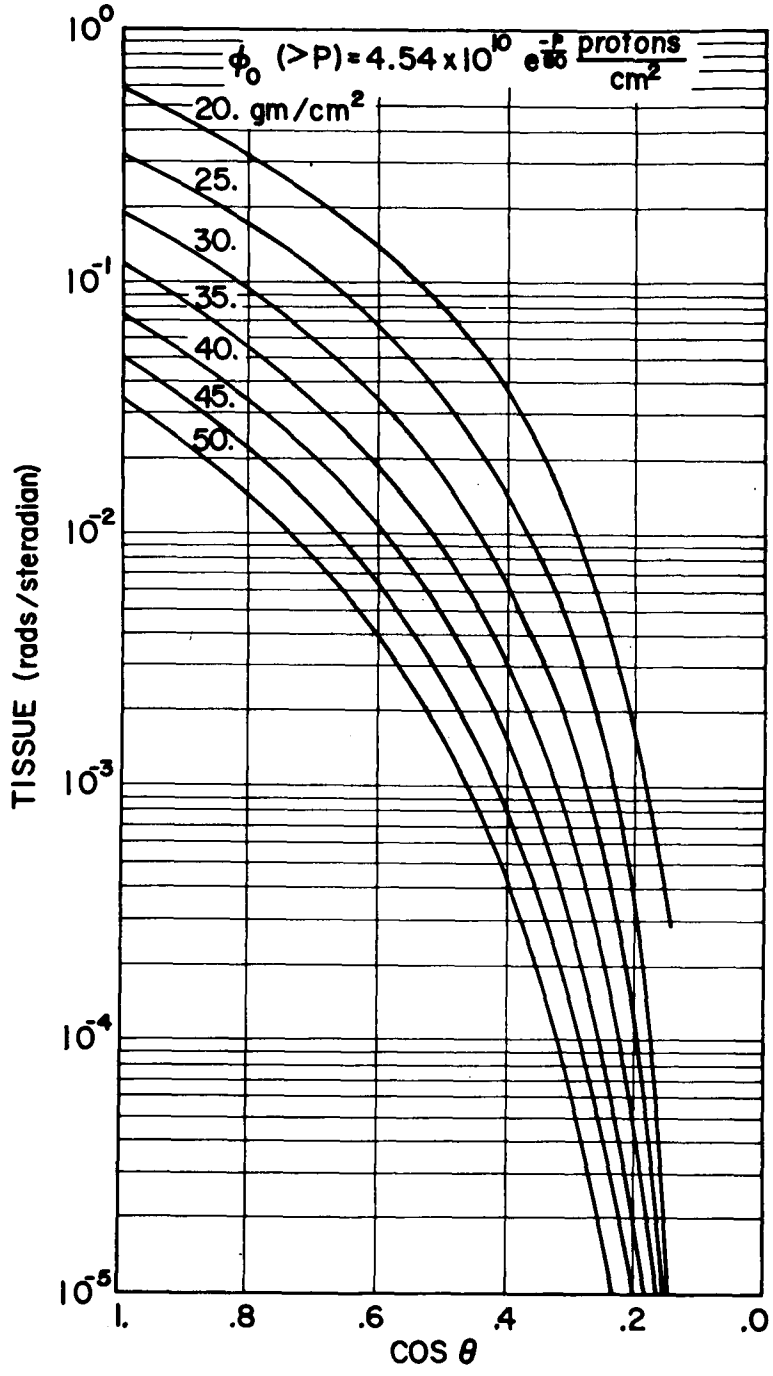

FIGURE 33. PROTON DOSE PER STERADIAN FOR ISOTROPIC INCIDENT FLUX ON SLAB OF ALUMINUM AT DIFFERENT DEPTHS

work [5] . The agreement seems rather good. Figures 28 and 29 are presented to parallel the treatments given in the previous chapters of this report for the same incident rigidity spectrum. Of course, the differential flux and dose/Mev are defined the same as previously excepting that an integration was performed over direction for the isotropic slab case. Figure 30 presents the double integration of Eq. (83) for the same incident flux as shown in Figs. 28 and 29. Figure 31 is presented merely to emphasize the difference between two geometries and compare the primary dose of Fig. 18 with that of Fig. 30. It should be noted that at $X = 0$ gm/cm^2 depth, the isotropic dose on a slab is 1/2 the dose at the center of a sphere. Thus, there is a systematic difference of a factor of two due to the difference of a 2π space and a 4π space in the inferred solid angle integration. Figures 32 and 33 complete the isotropic incidence analysis. Here the dose/steradian is presented for several thicknesses of aluminum ranging from 1 gm/cm^2 to 50 gm/cm^2 in Fig. 33. The possible applications of this type data are probably small since the straight-ahead model used in proton penetration calculations permits fairly simple numerical methods for even complex geometries. However, the curves do indicate the relative significance of the direction of incidence on the primary proton dose in finite slabs. The integration over solid angle of these curves gives the data points shown in Fig. 30. The curves in Figs. 32 and 33 indicate clearly that care should be exercised in an arbitrary assumption such as any proton with an angle of incidence greater than 45° to the normal can be ignored. For example, even for 10 gm/cm^2, one would probably feel it necessary to consider angles as large as 70° ($\cos\theta = .34$) in order to obtain a reliable integration over angle. The implications of Figs. 32 and 33 on the treatment of complex geometries leads one to recognize that relatively large proton fluxes may enter a detector at rather oblique angles measured from the vehicle surface normal, particularly if the vehicle walls are relatively thin. A study of more complex geometry effects is given by the writer in the report "Flare Proton Doses Inside Lunar Structures" [7] . Three examples taken from this report are shown in Figs. 34 and 36. The incident proton flux in these calculations was assumed to be isotropic and the rigidity spectrum $N(>p) = 4.54 \times 10^{10} \; e^{-P/80}$ used throughout this report was assumed. The dose calculations in Figs. 34, 35, and 36 are based on the "Total Estimated Dose," which includes secondaries.

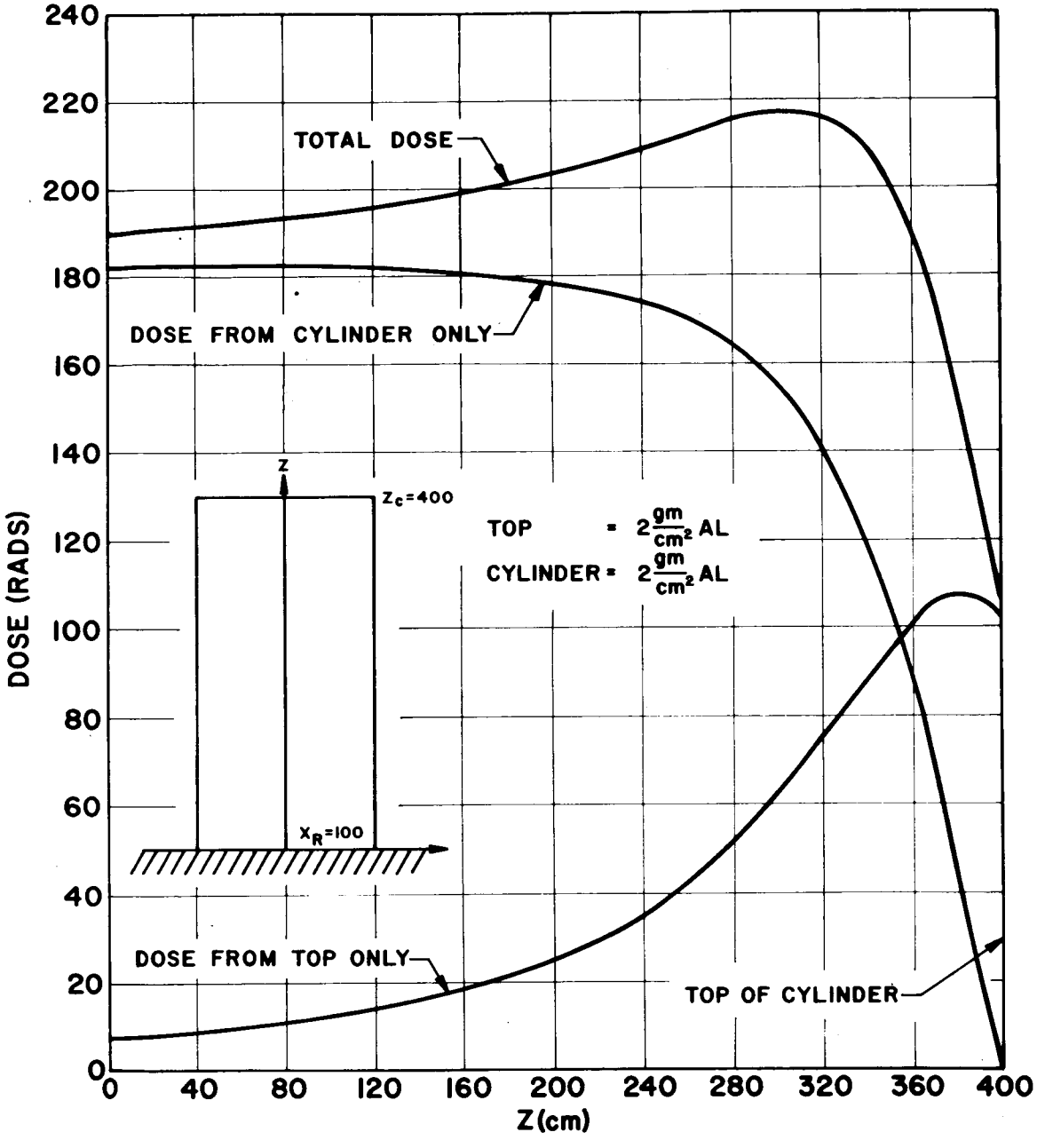

FIGURE 34. CENTER LINE DOSE VS. DISTANCE FROM BASE OF FLAT TOP CYLINDER

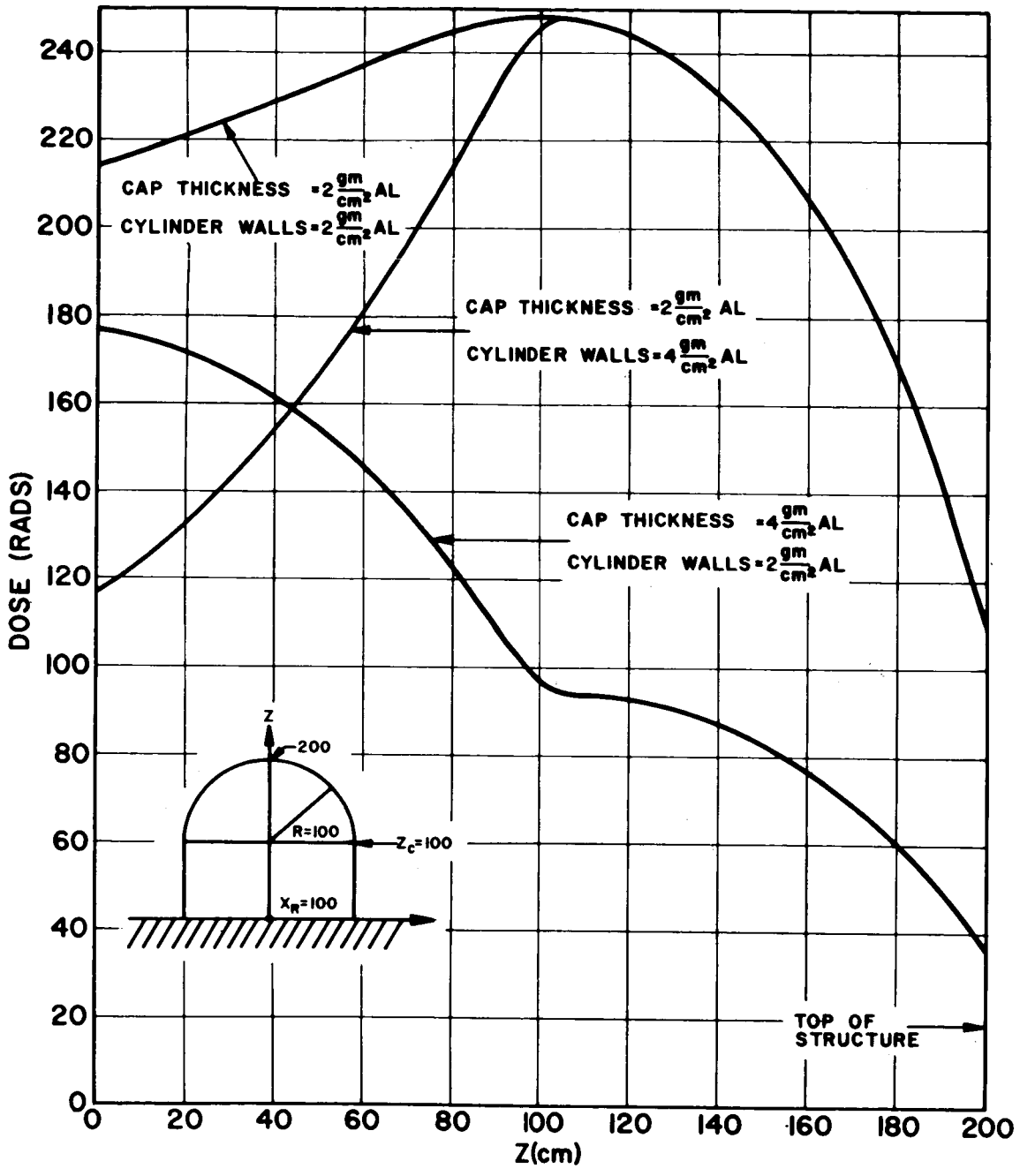

FIGURE 35. CENTER LINE DOSE VS. DISTANCE FROM BASE OF CYLINDER WITH SPHERICAL CAP

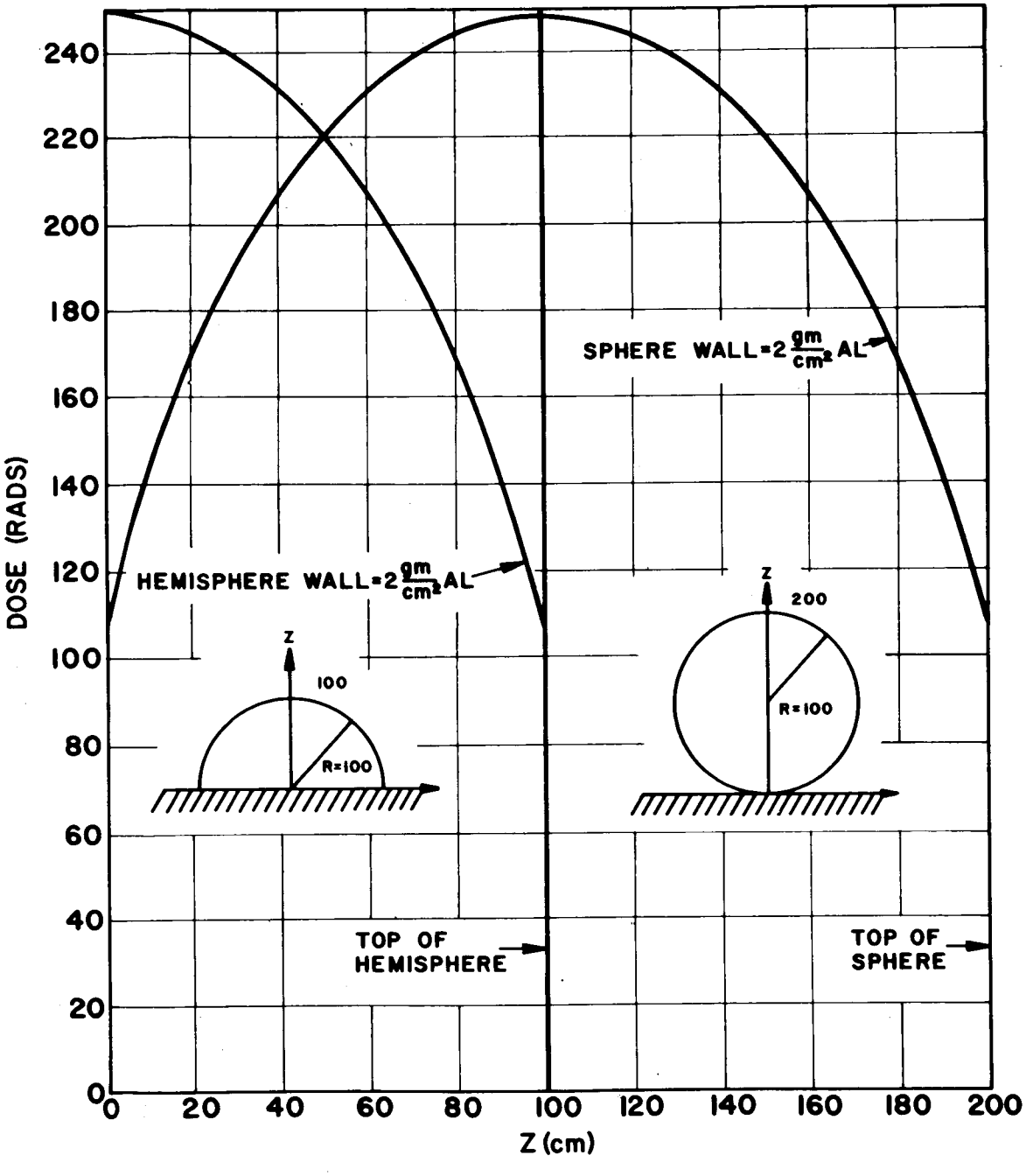

FIGURE 36. AXIS DOSE VS. DISTANCE FROM GROUND OF HEMISPHERE AND SPHERE

VII. CONCLUSIONS

One of the difficulties in an analysis of the type presented in the preceding pages is finding a point at which to stop. There are several areas which have been mentioned but not subjected to adequate study. For example, the examination of multiple layer shields and depth dose in tissue, as well as the tedious problem of treating secondary particle production fractions and their attenuation in a shield. However, it is hoped that usable short cuts and insight into various aspects of proton shielding have been made. Also, it is hoped that adequate information has been presented in the report for determining the validity of the results obtained and the scope of applications of the suggested approximations.

The computer codes used in the foregoing work are written in Fortran and are available to anyone interested. The proton dose rate code is capable of treating up to ten layers of different materials and takes directly either the coefficients of the integral rigidity spectrum (P in Million volts) or the power law representation of the differential spectrum (protons/cm^2-Mev-sec). The power law spectrum can be broken into as many as ten segments or energy groups. The output is rather extensive depending on the users' needs. Thus, differential flux, dose, and nonelastic collision density can be found as a function of the proton's energy inside the shield. If a choice is made to treat isotropic incidence of protons on a slab, the angular distribution of the transmitted proton dose is printed out for up to 20 increments in the angle θ measured from the slab normal. The greatest virtue of the above codes is the lack of large amounts of input data since the approximations discussed in this report are utilized wherever there is no real compromise in accuracy.

REFERENCES

1. Sternheimer, R. M., "Range-Energy Relations for Protons in Be, C, Al, Cu, Pb, and Au," Phys. Rev., 115, 137, 1959.

2. Hill, C. W., et al., "Computer Programs for Shielding Problems in Manned Space Vehicles," ER-6643, Lockheed-Georgia Company, January 1964.

3. Evans, Robley D., The Atomic Nucleus, McGraw-Hill Book Co., Inc., New York, 1955.

4. Troubetzkoy, E. S., "Fast Neutron Cross Sections of Iron, Silicon, Aluminum, and Oxygen," Nuclear Development Corp. of America, NDA 2111-3, Vol. C, November 1959.

5. Alsmiller, et al., 'From Neutron Physics Div., Space Radiation Shielding Research Annual Progress Report, August 31, 1962, pp. 148-155 (paper 1-10) ORNL 62-10-29.

6. Webber, W. R., "An Evaluation of the Radiation Hazard Due to Solar Particle Events," Boeing Report (D 2-90469), December 1963.

7. Burrell, M. O. and Watts, J. W., "Flare Proton Doses Inside Lunar Structures," Marshall Space Flight Center Internal Note, R-RP-INN-64-16, May 1964.

APPROVAL TM X-53063

THE CALCULATION OF PROTON PENETRATION AND DOSE RATES

by

Martin O. Burrell

. The information in this report has been reviewed for security classification. Review of any information concerning Department of Defense or Atomic Energy Commission programs has been made by the MSFC Security Classification Officer. This report, in its entirety, has been determined to be unclassified.

This document has also been reviewed and approved for technical accuracy.

Ernst Stuhlinger

ERNST STUHLINGER
Director, Research Projects Laboratory

DISTRIBUTION

DIR

Dr. von Braun

R-RP

Dr. Stuhlinger
Mr. Heller
Dr. Shelton
Dr. Dozier
Dr. Johnson
Dr. Mechtly
Mr. Miles
Mr. Cannon
Mr. Bucher
Mr. Urban
Dr. Ashley
Dr. Seitz
Dr. Hale
Dr. Edmonson
Mr. Stern
Mr. Prescott
Mr. McGlathery
Mr. Wright
Mr. Potter
Mr. Wood
Mr. King
Mr. Burrell (15)
Reserve (25)

R-AERO

Dr. Geissler

R-ASTR

Dr. Haeussermann

R-COMP

Dr. Hoelzer

R-P&VE

Mr. Cline

R-ME

Dr. Kuers

R-QUAL

Dr. Grau

R-TEST

Mr. Heimburg

MS-IPL (8)

MS-IP

MS-IS (6)

MS-H

HME-P

CC-P

Scientific and Technical
Information Facility (25)
Attn: NASA Representative
(S-AK/RKT)
P. O. Box 5700
Bethesda, Maryland

Space Nuclear Propulsion Off.
U. S Atomic Energy Commission
Washington 25, D. C.
Attn: Mr. Schwenk